nature cardiovascular research

ARTICLES

https://doi.org/10.1038/s44161-022-00046-4

Check for updates

A high-efficiency AAV for endothelial cell transduction throughout the central nervous system

Trevor Krolak[1,3], Ken Y. Chan[2,3], Luke Kaplan[1], Qin Huang[2], Jason Wu[2], Qingxia Zheng[2], Velina Kozareva[2], Thomas Beddow[2], Isabelle G. Tobey[2], Simon Pacouret[2], Albert T. Chen[2], Yujia A. Chan[2], Daniel Ryvkin[1], Chenghua Gu[1]✉ and Benjamin E. Deverman[2]✉

Endothelial cells have a crucial role in nervous system function and mounting evidence points to endothelial impairment as a major contributor to a wide range of neurological diseases; however, tools to genetically interrogate these cells in vivo remain limited. Here, we describe AAV-BI30, a capsid that specifically and efficiently transduces endothelial cells throughout the central nervous system. At relatively low systemic doses, this vector transduces the majority of arterial, capillary and venous endothelial cells in the brain, retina and spinal cord vasculature of adult C57BL/6 mice. Furthermore, we show that AAV-BI30 robustly transduces endothelial cells in multiple mouse strains and rats in vivo and human brain microvascular endothelial cells in vitro. Finally, we demonstrate the capacity of AAV-BI30 to achieve efficient and endothelial-specific Cre-mediated gene manipulation in the central nervous system. This combination of attributes makes AAV-BI30 well suited to address outstanding research questions in neurovascular biology and aid the development of therapeutics to remediate endothelial dysfunction in disease.

Recent strides in adeno-associated virus (AAV) development have produced engineered capsids capable of transducing well-defined cellular populations in the central nervous system (CNS) far more efficiently than their naturally occurring counterparts[1–7]. Leveraged as a rapid and flexible in vivo gene transfer platform, these vectors are poised to act as transformative catalysts for research when used in conjunction with (or as a substitute for) existing mouse genetics tools. However, capsid development has predominantly focused on vectors designed to transduce neurons or astrocytes. By comparison, relatively few vectors have been described that specifically target other cellular populations within the CNS, despite emerging appreciation that a vast repertoire of non-neuronal cell types is critical for nervous system function.

Among these, CNS endothelial cells (specialized cells that line the luminal face of blood vessels) have been shown to orchestrate a number of key physiological processes. Moreover, their dysfunction is increasingly appreciated to contribute to a wide range of neurodegenerative and neurological diseases[8,9]. While endothelial cells are often regarded as a relatively homogenous entity, recent work has highlighted a striking degree of molecular and functional specialization across the cerebrovascular arterio–venous axis[10]. For example, arterial endothelial cells play a critical role in dynamically coupling blood flow with neural activity to meet local energetic demand[11–13], capillary endothelial cells actively suppress transcytotic trafficking to maintain blood–brain barrier integrity[14–16] and venous endothelial cells appear to act as essential intermediaries in neuroimmune crosstalk[9,17,18]. However, a mismatch between the expanding functions ascribed to endothelial cells and the relatively limited tools available to study them in vivo is a major obstacle to research progress. A highly efficient, endothelial-specific vector with broad tropism encompassing arterial, capillary and venous endothelial cells would be ideally suited to accelerate neurovascular research. Similarly, the ability to effectively transduce spinal cord and retinal vasculature (widely studied systems in the field of neurovascular biology) in addition to brain vasculature would dramatically expand the applications of a CNS-directed, endothelial-specific vector.

To date, only two viral vectors with the ability to efficiently transduce cerebrovascular endothelial cells have been described, AAV-PHP.V1 (ref. [6]) and AAV-BR1 (ref. [2]), both of which have limitations that restrict their use. Within the brain, AAV-PHP.V1 does not selectively transduce endothelial cells; it transduces astrocytes with similarly high efficiency. Because astrocytes are intimately associated with the brain vasculature, this lack of specificity limits the vector's utility. AAV-BR1, by contrast, transduces brain microvascular endothelial cells with high specificity and has been successfully leveraged by a number of groups since its initial discovery[19–26]. However, while it is well established that AAV-BR1 efficiently transduces capillary endothelial cells, it is unclear whether the vector robustly targets the endothelium of arteries and veins. A recent study found that the efficacy of AAV-BR1 is diminished in these larger vessel segments[20], suggesting that it is not well suited to address rapidly emerging interest in the specialized functions of arterial and venous endothelial cells. Moreover, the vector's ability to effectively target spinal cord and retinal vasculature is ambiguous. Initial characterization of AAV-BR1 revealed that its transduction of the spinal cord endothelium was significantly less efficient than that observed in the brain[2] and while there is some evidence that the vector transduces endothelial cells of the retinal vasculature, its performance in this context remains poorly characterized[23].

Here, we describe a viral capsid that meets the need for a specific, high-efficiency vector to target endothelial cells throughout the entire CNS: AAV-BI30, an engineered variant of AAV9. At relatively low systemic doses in adult mice, this capsid transduces the majority of endothelial cells across the arterio–venous axis in brain, retina

[1]Department of Neurobiology and Howard Hughes Medical Institute, Harvard Medical School, Boston, MA, USA. [2]Stanley Center for Psychiatric Research, Broad Institute of MIT and Harvard, Cambridge, MA, USA. [3]These authors contributed equally: Trevor Krolak, Ken Y. Chan.
✉e-mail: Chenghua_Gu@hms.harvard.edu; bdeverma@broadinstitute.org

and spinal cord vasculature. Furthermore, we demonstrate that the capsid's transduction profile extends across species: we observed robust endothelial transduction in C57BL/6 and BALB/cJ mouse strains, in rats and in human brain microvascular endothelial cells. Finally, we show that the capsid can be utilized for efficient endothelial cell-specific Cre recombination and gene knockout in the brain vasculature. Taken together, these attributes make AAV-BI30 exceptionally well suited to accelerate our understanding of neurovascular interactions in normal physiology and to pioneer therapies to address their dysfunction in disease.

Results

AAV-BI30 transduces brain endothelial cells in mice and rats in vivo. To develop capsids with improved transduction of CNS endothelial cells, we generated an AAV9 capsid library and selected for capsids that more efficiently transduced human and mouse endothelial cells. The library comprised AAV9 variants modified with a randomized 7-mer insertion between amino acids 588 and 589 (AAV9 VP1 position). The library was built within a recombinant AAV backbone, AAV9-CMV-Express, which expresses the capsid gene in transduced cells. By sequencing capsid messenger RNA (mRNA) this approach allows for the selective recovery of functional capsids, eliminating AAV variants that traffic to the tissue or organ of interest but fail to achieve transgene expression. Similar RNA-based selection methods have recently been used to identify capsids with enhanced blood–brain barrier penetrance[7] and muscle transduction[27].

Using AAV9-CMV-Express, we selected for capsids expressed in human and mouse cells in vitro and in the brains of mice in vivo. After two rounds of selection, we identified a variant with the 7-mer amino acid sequence NNSTRGG that was enriched in the expressed capsid pool across five assays: in immortalized human cerebral microvascular endothelial cell (hCMEC/D3) transduction, in human and mouse brain microvascular endothelial cell (BMVEC) transduction and in C57BL/6J and BALB/cJ mouse brain transduction in vivo (Supplementary Fig. 1). In contrast, AAV-PHP.eB (a previously described capsid with enhanced CNS transduction[4] selective to a subset of mice, including C57BL/6J[28,29]) was only enriched in C57BL/6J brain and BMVECs derived from this strain.

To individually assess the transduction characteristics of AAV-BI30, we used the capsid to package a single-stranded recombinant AAV2 reporter genome. AAV-BI30 transduced BMVECs from mouse (282- to 2,261-fold) and human (72- to 96-fold) more efficiently than AAV9 (Fig. 1a). In addition, AAV-BI30 transduced hCMEC/D3 (22.7 ± 1.4-fold; mean ± s.d.) more efficiently than AAV9, an increase that was observed across a wide range of doses (Extended Data Fig. 1 and Supplementary Fig. 2). Fitting with our library enrichment data, this cross-species transduction enhancement differentiates AAV-BI30 from AAV-PHP.eB, which exhibited an enhanced transduction phenotype restricted to mouse (Fig. 1a) and AAV-BR1, which was not found to transduce hCMEC/D3 cells more efficiently than its parental vector AAV2 (ref. [2]).

Next, to evaluate the performance of AAV-BI30 in vivo we used the capsid to package a genome expressing a nuclear localization signal-tagged green fluorescent protein from the ubiquitous CAG promoter (AAV-BI30:CAG–NLS–GFP). We then intravenously administered the AAV at 1×10^{11} viral genomes (vg) per mouse in C57BL/6 mice and assessed transduction after 10 d. Encouragingly, AAV-BI30 transduced endothelial cells throughout the brain with remarkable efficiency and specificity at this dose (Fig. 1b, Extended Data Fig. 2 and Supplementary Fig. 3).

However, approximately 1 week after administration, we observed unexpected dose-dependent toxicity at doses as low as 1×10^{11} vg per mouse. This adverse response manifested in weight loss, lethargic behavior and ultimately mortality at the highest dose tested, 1×10^{12} vg per mouse. Necropsy revealed strong transduction of liver hepatocytes accompanied by abnormal nuclear morphology (Fig. 1c). To determine whether toxic overexpression of the NLS transgene in hepatocytes contributed to systemic toxicity, we incorporated three repeats of a hepatocyte-specific microRNA (miRNA) target sequence, miR122[30], into the 3′ untranslated region of our viral construct; a strategy successfully employed by a number of groups to selectively degrade transgene mRNA in hepatocytes[31–33].

This modification efficiently suppressed hepatocyte expression of the NLS–GFP transgene and prevented transient weight loss (Fig. 1d) without compromising AAV-BI30's transduction of the CNS vasculature, results consistent with virtually undetectable expression of *Mir122a* in brain endothelial cells[10]. A higher 5×10^{11} vg dose of AAV-BI30 carrying the modified NLS–GFP–miR122–WPRE construct similarly produced no discernible weight loss (Supplementary Fig. 4) illustrating the microRNA-binding element's ability to effectively de-target transgene expression from the liver across the experimental working range of the vector. Further, measuring less than 80 bp, the element did not constrain the functional packaging capacity of AAV-BI30. A survey of peripheral tissues following incorporation of the miR122 repeat element revealed transduction of several non-CNS endothelial populations in addition to hepatocytes, including endothelial cells in the lung microvasculature, aorta and interlobular vessels of the kidney (Extended Data Fig. 3). That said, the vector's transduction profile was strongly biased toward the CNS.

C57BL/6-restricted tropism has frustrated past efforts to deploy engineered AAV vectors in genetically intractable organisms[34,35]. To test whether the applications of AAV-BI30 were similarly constrained, we evaluated the capsid's performance in a second mouse strain (BALB/cJ) and a distinct mammalian species (rat). Consistent with the cross-species transduction of AAV-BI30 observed in vitro, the capsid achieved robust endothelial transduction in the BALB/cJ and rat brain following systemic administration (Fig. 1e and Extended Data Fig. 4).

AAV-BI30 transduces endothelial cells across the entire arterio–venous axis. We subsequently sought to assess the transduction efficiency of AAV-BI30 in brain endothelial cells. Previous studies have quantified the efficiency of endothelial-targeted vectors by measuring the colocalization of a viral transgene with endothelial-specific markers such as CD31 or GLUT1 (refs. [2,6]). This strategy relies on an implicit assumption that the size and morphology of individual endothelial cells is roughly consistent throughout the CNS; a generalization that does not hold true across the arterio–venous axis[36]. To improve upon existing approaches, we developed an automated workflow to estimate endothelial transduction efficiency by measuring colocalization of NLS–GFP with ERG, an endothelial-specific transcription factor[10,37]. Because ERG expression is sharply restricted to the nucleus, this strategy enabled fast and reliable identification of individual endothelial cells throughout the brain microvasculature (Fig. 1f).

Observing that the tropism of AAV-BI30 resembled that of AAV-BR1, despite its highly divergent sequence, we used this approach to directly compare the vectors and identify capsid-specific properties. Quantifying transduction across entire sagittal brain sections, we found that AAV-BI30 transduced 84 ± 4% (mean ± s.e.m.) of brain endothelial cells at 1×10^{11} vg per mouse. By comparison, AAV-BR1 transduced 66 ± 2% of this population at the same dose, consistent with previous reports[2,19,20,24] (Fig. 1g). The efficacy of AAV-BI30 showed no appreciable region-to-region variation throughout the brain; the cortex, hippocampus, thalamus and cerebellum all exhibited >80% endothelial cell transduction (Extended Data Fig. 5). Further, the vector was highly endothelial-specific in this dose regime; isolated instances of neuronal or astrocytic transduction were rare (Extended Data Fig. 6). Notably, while both AAV-BI30 and AAV-BR1 were predominantly endothelial-directed, AAV-BI30 transduced significantly fewer non-endothelial

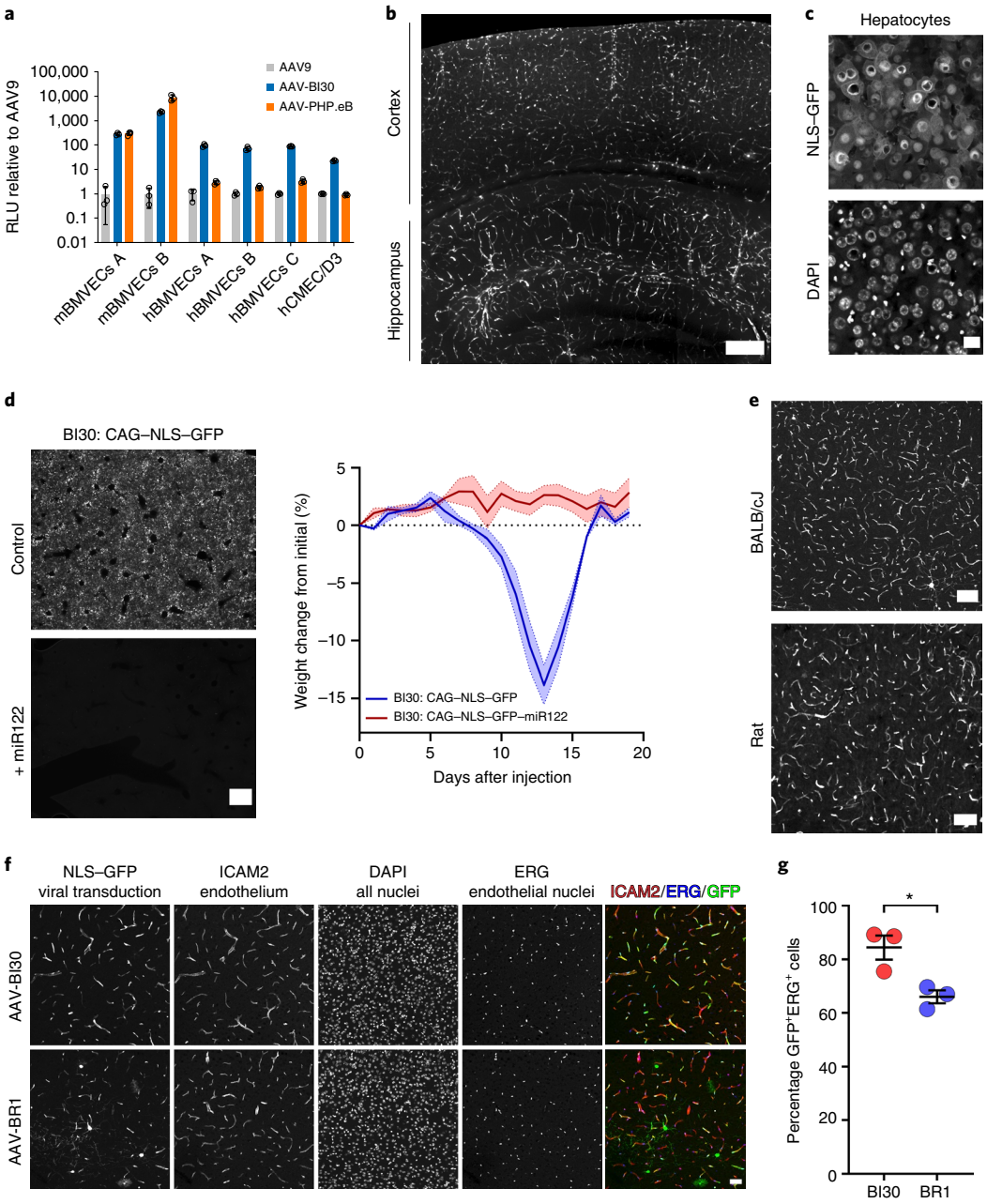

Fig. 1 | AAV-BI30 enables efficient transduction of brain endothelial cells across species. a, Quantification of transduction by AAV-BI30 and AAV-PHP.eB relative to AAV9 in several independent batches of mouse and human BMVECs and hCMEC/D3s assessed by luciferase activity (RLU). RLU, relative light units. **b**, Representative image of AAV-BI30 transduction in a sagittal section of adult C57BL/6 brain cropped to show cortex and hippocampus. Samples were collected 10 d after administration of 1×10^{11} vg per animal of AAV-BI30 carrying a CAG–NLS–GFP–WPRE genome. **c**, High-magnification images of mouse liver collected 10 d following intravenous injection of 3×10^{11} vg per animal of AAV-BI30. Note abnormal nuclear morphology in hepatocytes expressing the highest levels of GFP. DAPI, 4,6-diamidino-2-phenylindole. **d**, AAV-BI30 carrying a CAG–NLS–GFP–WPRE or CAG–NLS–GFP–miR122–WPRE genome was intravenously injected into adult C57BL/6 mice at 1×10^{11} vg per animal. Low-magnification images of liver collected 10 d after injection, demonstrating effective miR122-mediated suppression of transgene expression in hepatocytes (left). Starting immediately after viral injection, mice were weighed every 24 h for 20 consecutive days (mean ± s.e.m.; $n=3$ animals per group) (right). **e**, AAV-BI30:CAG–NLS–GFP–miR122–WPRE was intravenously administered at 1×10^{11} vg per animal (BALB/cJ) or 1.42×10^{13} vg kg^{-1} (rat). Transduction was assessed after 3 (BALB/cJ) or 4 (rat) weeks. Representative images show AAV-BI30 transduction in the cortical microvasculature of each animal. **f**, AAV-BI30 or AAV-BR1 carrying a CAG–NLS–GFP–miR122–WPRE construct were intravenously administered to adult C57BL/6 mice at 1×10^{11} vg per animal. Transduction was assessed after 3 weeks. Representative confocal images of viral transduction in cerebral cortex; note the high cell-type specificity of ERG immunostaining. **g**, Quantification of endothelial transduction measured as the fraction of ERG$^+$ cells expressing GFP in whole sagittal sections of brain ($t_4=3.631$; $P=0.0221$). For quantification: $n=3$ animals per group, mean ± s.e.m.; unpaired, two-tailed Student's t-test (*$P<0.05$). Scale bars, 500 µm (**d**); 250 µm (**b**); 100 µm (**e**,**f**); 25 µm (**c**).

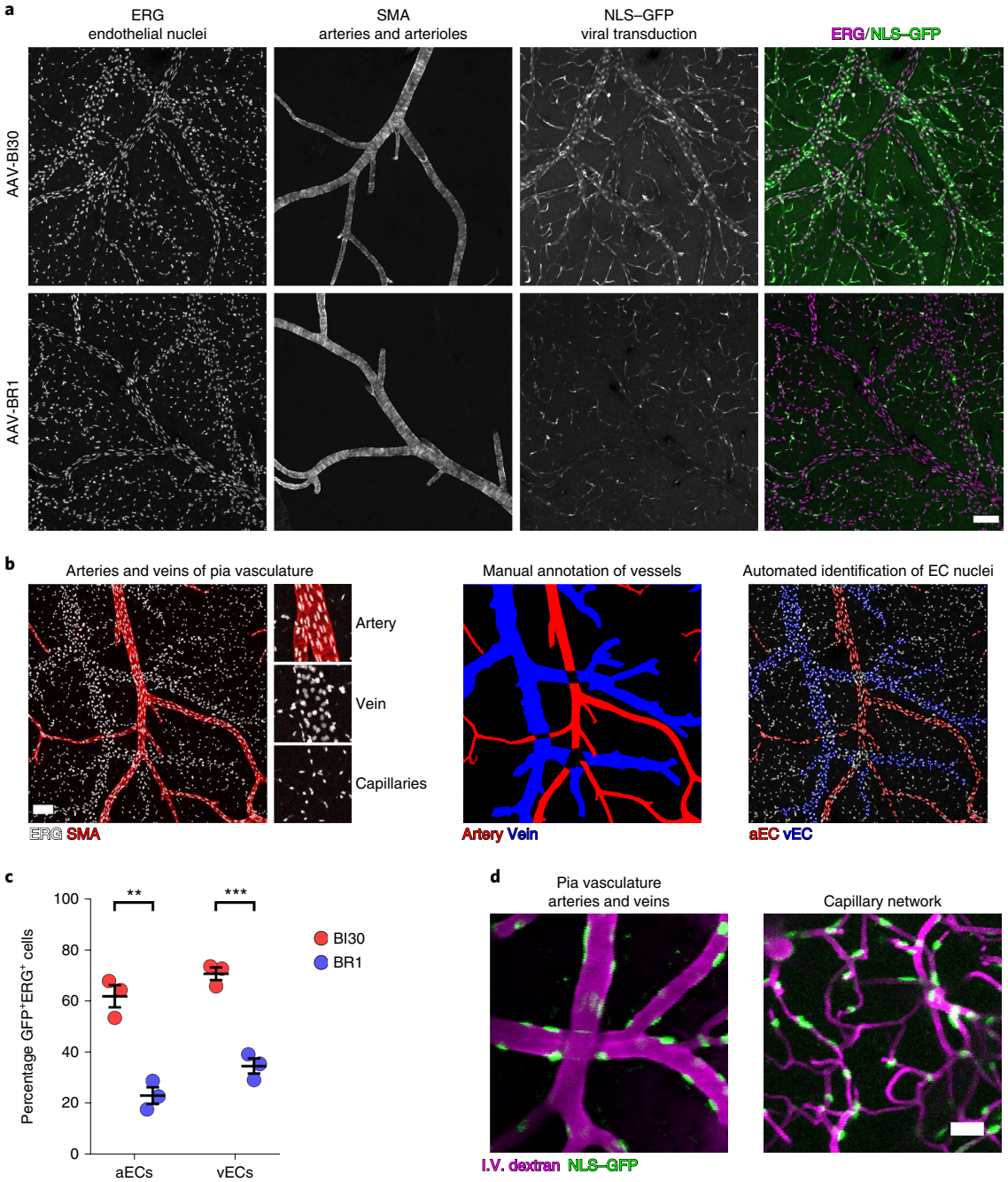

Fig. 2 | AAV-BI30 efficiently transduces brain endothelial cells across the arterio–venous axis. AAV-BI30 or AAV-BR1 carrying a CAG–NLS–GFP–miR122–WPRE construct was intravenously administered to adult C57BL/6 mice at 1×10^{11} vg per animal. Transduction was assessed after 3 weeks. **a**, Representative images of AAV-BI30 and AAV-BR1 transduction in whole-mount preparations of the pia vasculature. Note the strong GFP signal present in arteries, veins and capillaries following AAV-BI30 transduction; by contrast, GFP$^+$ endothelial cells transduced by AAV-BR1 are predominantly restricted to capillary microvessels. SMA, smooth muscle actin. **b**, Illustration of semi-automated image-processing workflow used to calculate arterial and venous transduction efficiency. Input image. Note that arteries, veins and capillaries are clearly separable on the basis of nuclear morphology of endothelial cells and α-SMA expression (left). Manual annotation of arteries and veins (middle). Artery–vein overlap regions were intentionally omitted from analysis. aEC and vEC nuclei identified by automated Cell Profiler pipeline superimposed on ERG channel of input image (right). aEC, arterial endothelial cell; vEC, venous endothelial cell; EC, endothelial cell. **c**, Quantification of endothelial transduction measured as the fraction of ERG$^+$ cells expressing GFP within manually annotated arterial ($t_4=7.172$; $P=0.0020$) and venous ($t_4=9.488$; $P=0.0007$) vessel segments. **d**, Representative two-photon z-stacks of brain vasculature imaged in live, awake mice demonstrate AAV-BI30's robust transduction of cerebrovascular arteries, veins and capillaries. I.V., intravenous. For quantification, $n=3$ animals per group, mean ± s.e.m.; unpaired, two-tailed Student's t-test ($^{**}P<0.01$, $^{***}P<0.001$). Scale bars, 100 µm (**a**,**b**) and 25 µm (**d**).

cells than AAV-BR1 (which is known to sporadically transduce neurons and astrocytes[2,38]).

Next, we measured the transduction efficiency of AAV-BI30 in endothelial cells of larger arteries and veins. While surveying sagittal or coronal sections is well suited to the gauge the overall efficiency of AAV transduction across the brain microvasculature, it provides limited information about a vector's ability to transduce different segments of the arterio–venous axis. Capillaries,

the brain's smallest blood vessels, constitute the vast bulk of the cerebrovascular network. Furthermore, arteries and veins are disproportionately confined to the pia surface and poorly sampled by sectioning approaches. As a result, the overwhelming majority of microvessels surveyed in a given sagittal or coronal plane are capillaries. Therefore, to assess the ability of AAV-BI30 and AAV-BR1 to target the endothelium of arteries and veins we examined whole-mount preparations of the intact pia vasculature (Fig. 2a). Because ERG is ubiquitously expressed across arteries, capillaries and veins our analysis workflow could be rapidly adapted to calculate segment-specific transduction efficiency. We manually identified arteries and veins based on (1) the presence of α-smooth muscle actin (high in arteries, low to absent in veins)[10,39] and (2) the nuclear morphology of endothelial cells (ellipsoidal in arteries and circular in veins)[36] (Fig. 2b). Notably, we found that AAV-BI30 captured these vessel segments efficiently, transducing 62 ± 4% of arterial endothelial cells and 71 ± 3% of venous endothelial cells. By contrast, AAV-BR1's tropism seemed strongly biased against large-vessel transduction: the vector only transduced 23 ± 3% of arterial endothelial cells and 35 ± 3% of venous endothelial cells in the pia vasculature (Fig. 2c). In line with these findings, we were able to visualize robust AAV-BI30-mediated endothelial GFP expression in the arteries, capillaries and veins of live mice via two-photon imaging through surgically implanted cranial windows (Fig. 2d). Of note, the tropism of AAV-BI30 extended to the largest arteries of the brain; at a higher dose (5×10^{11} vg per mouse) we observed efficient endothelial transduction throughout the circle of Willis and associated cerebral arteries (Extended Data Fig. 7). Collectively, these results demonstrate that AAV-BI30 can be leveraged to genetically interrogate the majority of brain endothelial cells across the entire arterio–venous axis at relatively low systemic doses.

AAV-BI30 transduces endothelial cells in retina and spinal cord. While the majority of endothelial-targeted AAV research to date has focused on the brain vasculature, the retina and spinal cord vasculature are highly tractable systems crucial to the study of angiogenesis, blood–brain barrier dynamics, neurovascular pathology and a host of other key processes[16,40–42]. Accordingly, we investigated AAV-BI30's capacity to transduce the endothelial cells of these CNS tissues. Across all segments of the retina's stereotyped vasculature, AAV-BI30 dramatically outperformed AAV-BR1, transducing 73 ± 3% versus 14 ± 3% superficial plexus arterial endothelial cells; 69 ± 4% versus 18 ± 1% intermediate plexus endothelial cells; 75 ± 3% versus 30 ± 5% deep plexus endothelial cells; and 81 ± 4% versus 23 ± 2% superficial plexus venous endothelial cells (Fig. 3a–c). The difference between the vectors was similarly apparent in the spinal cord, where AAV-BI30 transduced 76 ± 4% of endothelial cells compared to AAV-BR1's 46 ± 5%, an estimate consistent with the capsid's initial characterization[2] (Fig. 3d,e). Thus, AAV-BI30's highly efficient, endothelial cell-specific tropism is not limited to the brain; instead, it extends the entirety of the CNS. In addition, AAV-BI30-mediated transgene expression persists across long timescales. We observed robust endothelial transduction in brain, retina and spinal cord 152 d after administration of a single 1×10^{11} vg dose of the vector (Extended Data Fig. 8); a result consistent with the relatively slow turnover of CNS endothelial cells[43] and longitudinally stable endothelial transduction previously demonstrated with AAV-BR1 (ref. [2]).

AAV-BI30 can be leveraged for brain endothelial-specific gene manipulation. To evaluate the capacity of AAV-BI30 to genetically manipulate CNS endothelial cells in vivo, we used the capsid to package Cre recombinase (AAV-BI30:CAG–Cre–miR122–WPRE) and delivered a 1×10^{11} vg dose of the vector to *Rosa26:CAG-LSL-tdTomato* (Ai9) Cre-dependent reporter mice[44]. Consistent with our previous results, we observed remarkably efficient, endothelial-specific tdTomato expression throughout the brain (Fig. 4a,b and Supplementary Fig. 5). By quantifying ERG colocalization with tdTomato (Fig. 4c), we found that AAV-BI30-mediated Cre delivery drove recombination in 94 ± 1% of endothelial cells within the cortical microvasculature.

We next tested this strategy's ability to achieve acute genetic loss of function in CNS endothelial cells. For a proof of concept we chose to target caveolin-1 (encoded by the *Cav1* gene), an essential component of caveolae[45]. Caveolae are flask-shaped vesicular invaginations of the plasma membrane found in a number of cell types, including endothelial cells. Within CNS endothelial cells, these subcellular structures play a key role in blood–brain-barrier dynamics[15,16] and neurovascular coupling[13] among other important functions.

To genetically ablate caveolin-1 expression, we delivered a 1×10^{11} vg dose of AAV-BI30 carrying a CAG–Cre–miR122–WPRE genome to $Cav1^{fl/fl}$ mice[46]. Four weeks after administration we observed strong reduction of caveolin-1 protein in the brain endothelial cells of AAV-BI30-injected animals relative to saline-injected controls (Fig. 4d). Notably, this effect was brain endothelial cell-specific; protein levels in arterial smooth muscle cells, which also express high levels of caveolin-1 (refs. [10,13]), were unaltered following AAV-BI30 administration (Extended Data Fig. 9). Consistent with our results in the Ai9 reporter line, we saw a small population of endothelial cells that escaped transduction in the 1×10^{11} vg dose regime with no apparent reduction in caveolin-1 expression. By titrating dosage, experimenters could use AAV-BI30 to achieve mosaic recombination; an approach that would be particularly useful to investigate the cell-autonomous function of blood–brain-barrier genes whose widespread loss throughout CNS endothelial cells is lethal, such as claudin-5 (ref. [47]) or β-catenin[48–51].

In addition, we verified that AAV-BI30-mediated Cre delivery did not drive widespread loss of endothelial caveolin-1 outside of the CNS. Protein levels in the heart microvasculature (an organ where endothelial caveolin-1 is known to be robustly expressed[52]) were not appreciably altered in AAV-BI30-injected animals (Fig. 4e). Given that no CNS endothelial cell-specific transgenic drivers currently exist, the ability to rapidly perform CNS-directed loss-of-function experiments may make AAV-BI30-mediated Cre delivery an attractive alternative to commonly used pan-endothelial driver lines such as *CDH5:Cre*^{ERT2} (ref. [53]) or *TIE2:Cre* (ref. [54]).

Fig. 3 | AAV-BI30 targets endothelial cells throughout the retina and spinal cord vasculature. AAV-BI30 or AAV-BR1 carrying a CAG–NLS–GFP–miR122–WPRE construct was intravenously administered to adult C57BL/6 mice at 1×10^{11} vg per animal. Transduction was assessed after 3 weeks. **a**,**b**, Representative low (**a**) and high (**b**) magnification images of AAV-BI30 and AAV-BR1 transduction in retina are shown. **c**, Quantification of retinal endothelial transduction measured as the fraction of ERG$^+$ cells expressing GFP in superficial plexus (SP) arteries ($t_4 = 13.05$; $P = 0.0002$), intermediate plexus (IP) vessels ($t_4 = 11.44$; $P = 0.0003$), deep plexus (DP) vessels ($t_4 = 8.107$; $P = 0.0013$) and SP veins ($t_4 = 12.45$; $P = 0.0002$). **d**, Representative images of AAV-BI30 and AAV-BR1 transduction in spinal cord; high-zoom colocalization of GFP with endothelial markers is shown in bottom row. **e**, Quantification of endothelial transduction measured as the fraction of ERG$^+$ cells expressing GFP in whole transverse sections of spinal cord ($t_4 = 4.815$; $P = 0.0086$). For quantification: $n = 3$ animals per group, mean ± s.e.m.; unpaired, two-tailed Student's *t*-test (**$P < 0.01$, ***$P < 0.001$). Scale bars, 100 μm (**a**,**d** left), 50 μm (**b**) and 25 μm (**d** right).

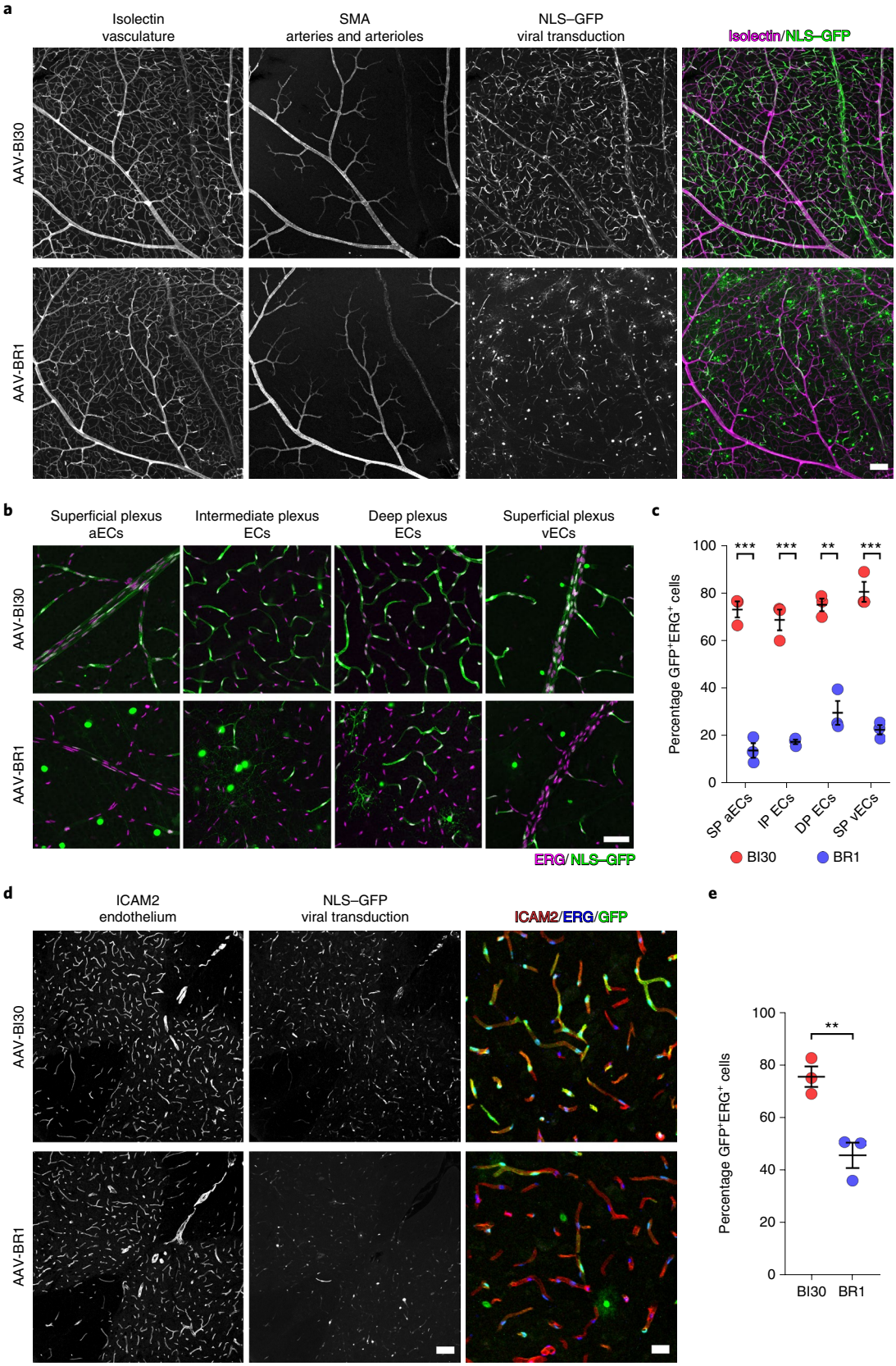

Discussion

Here we demonstrate that AAV-BI30 is ideally suited to accelerate neurovascular research, providing a rapid and easily adaptable means to access CNS endothelial cells with clear advantages over existing vectors (Extended Data Fig. 10). Unlike AAV-PHP.V1, at a 1×10^{11} vg dose the tropism of AAV-BI30 within the CNS is almost exclusively limited to endothelial cells, obviating the need for complex workarounds (such as intersectional Cre-dependent

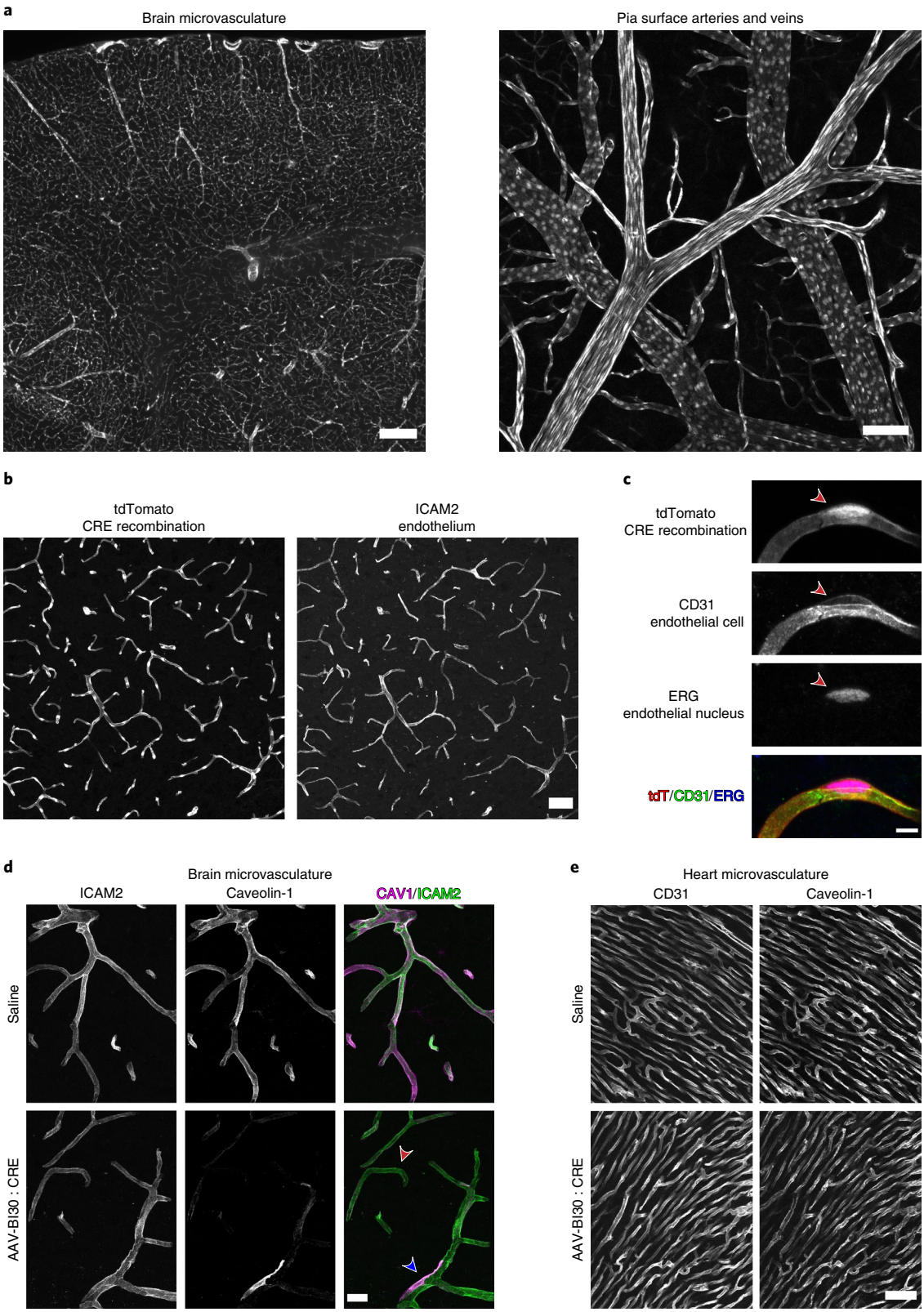

approaches) to restrict cell-type specificity. And compared to AAV-BR1, AAV-BI30 is more efficient and versatile, with particularly evident benefits for applications targeting retina, spinal cord or cerebrovascular arteries and veins.

While the tropism of AAV-BI30 seems largely biased toward the CNS vasculature, we observed transduction of liver hepatocytes and endothelial cells in the lung microvasculature, aorta and interlobular vessels of the kidney. Of note, peripheral endothelial transduction was sharply restricted to these populations (most organs had little-to-no endothelial cell transduction). For most research applications, the advantageous properties of AAV-BI30 likely outweigh this caveat. However, in cases where CNS-specificity is

Fig. 4 | AAV-BI30 can be leveraged to achieve efficient endothelial-specific genetic manipulation. a, AAV-BI30:CAG–Cre–miR122–WPRE was intravenously administered to adult Ai9 Cre-dependent reporter mice at 1×10^{11} vg per animal and recombination was assessed after 12 d. Robust tdTomato expression was observed throughout the brain microvasculature (left) as well as arteries and veins situated at the pia surface (right). **b**,**c**, Representative low (**b**) and high (**c**) magnification images of BI30-mediated Ai9 recombination in the cortical microvasculature; colocalization with endothelial-specific markers demonstrates cell-type-specificity. Recombination efficiency, measured as the fraction of ERG$^+$ cells expressing tdTomato, was 94 ± 1% (mean ± s.e.m.; $n = 3$ animals) in this brain region. **d**,**e**, A 1×10^{11} vg per animal dose of AAV-BI30:CAG–Cre–miR122–WPRE or saline was intravenously administered to adult Cav1$^{fl/fl}$ mice and caveolin-1 protein levels were assessed after 4 weeks by immunohistochemistry. Representative images of brain microvasculature demonstrate reduction of endothelial caveolin-1 in AAV-BI30-injected animals (**d**). The majority of endothelial cells in these animals exhibited a spectrum of moderate to near-complete protein loss (red arrow), likely reflecting variable viral genome count and consequent stage of protein turnover. A small fraction of endothelial cells showed no evidence of caveolin-1 loss (blue arrow). Representative images of caveolin-1 in heart microvasculature in AAV-BI30:CAG–Cre–miR122–WPRE and saline-injected mice (**e**). All images are representative of $n = 3$ animals per group. Scale bars, 250 µm (**a** left), 100 µm (**a** right), 50 µm (**b**,**e**), 20 µm (**d**) and 5 µm (**c**).

critical, a Cre-dependent viral genome could be used in tandem with a CNS-specific transgenic driver, such as *MFSD2A:Cre*^{ERT2} (ref. [55]) or *SLCO1C1:Cre*^{ERT2} (ref. [56]) to minimize the peripheral transduction of AAV-BI30 .

During our characterization of AAV-BI30 we encountered unexpected dose-dependent hepatoxicity. By incorporating a hepatocyte-specific miRNA-binding site into our viral genome, we were able to effectively rescue toxicity without compromising the vector's on-target transduction efficiency. This miRNA-based strategy functions by suppressing translation of the AAV transgene in hepatocytes without affecting stages of transduction involving the capsid protein; as a result, the strategy's efficacy argues against the possibility that the AAV-BI30 capsid's modifications have resulted in de novo immunogenicity. Instead, the hepatotoxicity observed in our study most likely stems from cytotoxic transgene overexpression[57,58]. Future engineering efforts could modify additional features of the AAV-BI30 capsid to limit hepatocyte transduction, similar to a recent study which generated a variant of the AAV-PHP.eB capsid de-targeted from peripheral organs[59]. Alternatively, the development of robust endothelial-specific promoters would likely obviate the need to include miRNA-binding sites in the viral genome. This latter approach could even be used to restrict transgene expression to one or more of the endothelial subpopulations transduced by AAV-BI30 in a manner similar to vessel segment-specific transgenic drivers like *BMX:Cre*^{ERT2} (ref. [60]).

In contrast with a number of recently discovered AAV vectors, including AAV-PHP.B[34] and AAV-PHP.V1 (ref. [6]), the transduction profile of AAV-BI30 was broadly similar between C57BL/6 and BALB/cJ mouse strains. The BALB/cJ strain's hypomorphic *Ly6a* allele has been directly linked to impaired CNS transduction by capsids of the AAV-PHP.B family following systemic administration[28,29,61]. As a result, our findings suggest that AAV-BI30's mechanism of transduction is LY6A-independent. We speculate that the virus may instead enter cells using a surface receptor present on endothelial cells throughout the body but enriched in CNS and lung microvasculature. Moving forward, recent efforts to profile the transcriptomes of endothelial cells isolated from a wide variety of murine organs[52] could be leveraged to identify candidate receptors.

AAV-BI30 seems well suited for a wide range of applications such as gene editing[62,63], live-imaging sensors, loss- and gain-of-function studies or two-component tunable expression systems[4]. The vector's high efficacy is likely understated by the binary quantification metric used throughout our analyses; throughout the brain, retina and spinal cord we observed a wide range of NLS–GFP intensities, suggesting that at a relatively low 1×10^{11} vg dose we delivered multiple viral genomes to a large number of CNS endothelial cells. Moreover, given that structural modifications to AAV capsids can dramatically reduce their manufacturability, it is important to note that when used to package a variety of genomes for this study (fluorescent reporters, bioluminescence producing enzymes and gene editors) post-purification AAV-BI30 yields were in line with other engineered and natural AAV vectors (Supplementary Fig. 6). This versatility (combined with the capsid's conserved tropism across mouse strains and mammalian species) highlights the potential of AAV-BI30 as a powerful tool to access CNS endothelial cells in vivo and catalyze our growing understanding of neurovascular processes in health and disease.

Methods

Animals. All procedures were approved by the Harvard University and Broad Institute of MIT and Harvard Institutional Animal Care and Use Committees. The following commercially available mouse strains were used: C57BL/6NCrl (Charles River 027), C57BL/6J (Jackson Laboratory 000664), BALB/cJ (Jackson Laboratory 000651) and Ai9 (Jackson Laboratory 007909; originally generated by Madisen et al.[44]). CD (Sprague Dawley) IGS rat was obtained from Charles River (strain code 001). *Cav1*^{flox} mice were originally generated by Asterholm et al.[46] and generously shared by P. Scherer. The line was genotyped using Phire Green Hot Start II DNA Polymerase (Thermo Fisher F124L) and the following primers: 5′-GTGCATCAGCCGCGTCTACTCC-3′ and 5′-GGCCGTAACCTGAATCTCTTCCCTTTG-3′. PCR reaction with genomic DNA samples produces ~490 bp wild-type and ~445 bp floxed products. Recombinant AAV vectors were administered intravenously via the tail vein or retro-orbital sinus in young adult male or female animals.

Virus production. Recombinant AAVs were generated following a previously published protocol[64] with minor modifications as described below. HEK293T/17 cells (ATCC, CRL-11268) were seeded at 22 million cells per 15-cm plate the day before transfection and grown in DMEM with GlutaMAX (Gibco, 10569010) supplemented with 5% FBS and 1× non-essential amino acid solution (NEAA) (Gibco, 11140050). The next day, the cells were triple transfected with 39.93 µg of total plasmid DNA encoding rep-cap, pHelper and an ITR-flanked transgene at a plasmid ratio of 4:2:1, respectively, using polyethylenimine (PEI) MAX (Polyscience, 24765-1) at a DNA:PEI ratio of 1:3.5. Twenty hours after transfection, the medium was changed to fresh DMEM with GlutaMAX supplemented with 5% FBS and 1× NEAA. Seventy-two hours after transfection, cells were scraped and pelleted at 2,000 RCF for 10 min. The pellets were resuspended in 7 ml of Salt Active Nuclease (SAN) digestion buffer (500 mM NaCl, 40 mM Tris-base, 10 mM $MgCl_2$, SAN enzyme (ArcticZymes, 70920-202) at 100 U ml^{-1}) for every ten plates and incubated at 37 °C for 1.5 h. Afterwards, the lysate was clarified at 2,000 RCF for 10 min and loaded onto a density step gradient containing OptiPrep (Cosmo Bio, AXS-1114542) at 60%, 40%, 25% and 15% at a volume of 5, 5, 6 and 6 ml, respectively in OptiSeal tubes (Beckman, 361625). The step gradients were spun in a Beckman Type 70ti rotor (Beckman, 337922) in a Sorvall WX+ ultracentrifuge (Thermo Fisher Scientific, 75000090) at 69,000 r.p.m. for 1 h at 18 °C. Afterwards, 4–4.5 ml of the 40–60% interface was extracted using a 16-gauge needle, filtered through a 0.22-µm PES filter and then buffer exchanged with 100 K MWCO protein concentrators (Thermo Fisher Scientific, 88532) into PBS containing 0.001% Pluronic F-68 and concentrated down to a volume of 500 µl. The concentrated virus was then filtered through a 0.22-µm PES filter and stored at 4 °C or −80 °C.

Virus titering. Purified virus was incubated with 1,000 U ml^{-1} Turbonuclease (Sigma T4330-50KU) with 1× DNase I reaction buffer (NEB B0303S) at 37 °C for 1 h. The endonuclease solution was inactivated with 0.5 M, pH 8.0 EDTA at room temperature for 5 min and then at 70 °C for 10 min. AAV genomes were released by incubation with 100 µg ml^{-1} Proteinase K (QIAGEN, 19131) in 1 M NaCl, 1% *N*-lauroylsarcosine and in UltraPure DNase/RNase-free water at 56 °C for 2 to 16 h before heat inactivation at 95 °C for 10 min. The nuclease-resistant AAV genomes were diluted between 460–460,000 times and 2 µl of the diluted samples was used as input in a ddPCR supermix for probes (Bio-Rad, 1863023)

with 900 nM ITR2_forward (5′-GGAACCCCTAGTGATGGAGTT-3′), 900 nM ITR2_reverse (5′-CGGCCTCAGTGAGCGA-3′) and 250 nM ITR2_probe (5′-HEX-CACTCCCTC-ZEN-TCTGCGCGCTCG-IABkFQ-3′). The ITR2_probe contained the following modifications: 5′ HEX dye, ZEN internal quencher and 3′ Iowa Black fluorescent quencher (IDT, PrimeTime qPCR Probes). Droplets were generated using a QX100 Droplet Generator, transferred to thermocycler and cycled according to the manufacturer's protocol with an annealing/extension of 58 °C for 1 min. Finally, droplets were read on a QX100 Droplet Digital System to determine titers.

In vitro transduction assays. Multiple lots of mBMVEC and hBMVEC cells were obtained from CellBiologics (H-6023 and C57-6023) and maintained in endothelial cell medium (H1168 and M1168). hCMEC/D3 cells were obtained from Millipore (SCC0066) and maintained in EndoGRO-MV Complete Media (SCME004). All cells were handled according to the manufacturer's instructions. For the luciferase assays, 5,000 cells per well were seeded in 96-well plates (PerkinElmer, 6005680). One day later, AAV9, AAV-PHP.eB or AAV-BI30 carrying pAAV–CAG–eGFP–p2A–luciferase was added at 20,000 vg per cell. At 24 h after transduction, a luciferase reporter assay was performed according to the manufacturer's instructions (PerkinElmer, 6066761) on an EnSpire plate reader (PerkinElmer). For flow cytometry, hCMEC/D3 cells were plated at 434,000 cells per well in 24-well plates and exposed to the indicated dose of AAV-BI30 or AAV9. The medium was exchanged for fresh medium after 24 h and transduction was assessed at 4 d after administration on a Beckman CytoFLEX S Flow Cytometer using FlowJo v.10.8.1 (BD Biosciences).

Capsid library generation. The mRNA selection vector (AAV9-CMV-Express) was designed to enrich for functional AAV capsid sequences by recovering capsid mRNA from transduced cells. AAV9-CMV-Express uses a ubiquitous CMV enhancer and AAV5 p41 gene regulatory elements to drive AAV9 Cap expression. The AAV9-CMV-Express plasmid was constructed by cloning the following elements into an AAV genome plasmid in the listed order: a cytomegalovirus (CMV) enhancer-promoter, a synthetic intron and the AAV5 P41 promoter along with the 3′ end of the AAV2 Rep gene, which includes the splice donor sequences for the capsid RNA. The capsid gene splice donor sequence in AAV2 Rep was modified from CAGGTACCA to a consensus donor sequence CAGGTAAGT. The AAV9 capsid gene sequence was synthesized with nucleotide changes at 1,344, 1,346 and 1,347 (which introduces a K449R mutation) and at 1,782 (which is a silent mutation) to introduce restriction enzyme recognition sites for NNK library PCR insert fragment cloning. The AAV2 polyadenylation sequence was replaced with a simian virus 40 (SV40) late polyadenylation signal. A previously described *cap*-deficient Rep-AAP AAV helper plasmid[1] was supplied in *trans* to generate virus with the AAV9-CMV-Express vector.

The initial random 7-mer library was produced using 5′-CGGACTCAGACTATCAGCTCCC-3′and 5′-GTATTCCTTGGTTTTGAACC CAACCGGTCTGCGCCTGTGCMNNMNNMNNMNNMNNMNNMNNTTGG GCACTCTGGTGGTTTGTG-3′ primers (IDT) to PCR amplify a modified AAV9 template (K449R) using Q5 Hot Start High-Fidelity 2× Master Mix (NEB, M0494S) following the manufacturer's protocol. The PCR products were cleaned up using AMPure XP beads (Beckman, A63881) following the manufacturer's protocol. The NNK PCR insert was assembled into a linearized mRNA selection vector (AAV9-CMV-Express) with NEBuilder HiFi DNA Assembly Master Mix (NEB, E2621L). Afterwards, Quick CIP (NEB, M0508S) was spiked into the reaction and incubated at 37 °C for 30 min to dephosphorylate unincorporated dNTPs. Finally, T5 Exonuclease (NEB M0663S) was added to the reaction mixture and incubated at 37 °C for 30 min to remove unassembled products. The final assembled product was cleaned up using AMPure XP beads (Beckman, A63881) following the manufacturer's protocol quantified using the Qubit dsDNA HS Assay Kit (Thermo Fisher Scientific, Q32851). Capsid variants chosen for secondary screening were synthesized as an oligopool (Agilent). Each capsid 7-mer was represented by two unique nucleotide sequences and cloned into the AAV9-CMV-Express backbone as described above.

Capsid library screening. For in vivo screening, the AAV capsid library was injected at 1×10^{11} vg per animal in either C57BL/6J or BALB/cJ mice. At 21 d after injection, animals were killed and tissue was extracted and flash-frozen for RNA isolation. For in vitro screening, 1×10^{11} vg of the AAV capsid library was added to confluent BMVECs or hCMEC/D3 cells and cellular mRNA was collected 3 d after administration. mRNA from in vivo and in vitro assays were recovered using TRIzol (Invitrogen, 15596026) followed by RNA cleanup with RNeasy Mini kit (QIAGEN, 74104). The recovered mRNA was next converted to complementary DNA using an oligonucleotide dT primer using Maxima H Minus Reverse Transcriptase (Thermo Fisher, EP0751). To prepare AAV libraries for sequencing, qPCR was performed on the converted cDNA from each sample type to identify the minimum number of cycles necessary for amplification. Once cycle thresholds were determined SeqF1 (5′-CTTTCCCTACACGACGCTCTTCCGATCTNCC AACGAAGAAGAA-ATTAAAACTACTAACCCG-3′) and SeqR1 (5′- GGAGTT CAGACGTGTGCTCTTCCGATCTCATCTCTGTCCTGCCA-AACCATACC-3′) primers were used to attach Illumina Read 1 and Read 2 sequences using Q5 Hot Start High-Fidelity 2× Master Mix with an annealing temperature of 65 °C for 20 s and an extension time of 1 min with a cycle number determined from the qPCR. These PCR products were purified using AMPure XP beads following the manufacturer's protocol and eluted in 25 µl UltraPure Water (Thermo Fisher Scientific) and then 2 µl was used as input in a secondary PCR to attach Illumina adaptors and dual index primers (NEB, E7600S) for five cycles using Q5 Hot Start-High-Fidelity 2× Master Mix with an annealing temperature of 65 °C for 20 s and an extension time of 1 min. The second PCR products were purified using AMPure XP beads following the manufacturer's protocol and eluted in 25 µl UltraPure DNase/RNase-free distilled water (Thermo Fisher Scientific, 10977015). To quantify the PCR product for next-generation sequencing, an Agilent High Sensitivity DNA kit (Agilent, 5067-4626) was used with an Agilent 2100 Bioanalyzer system. The secondary PCR products were then pooled and diluted to 2–4 nM in 10 mM Tris-HCl, pH 8.5 and sequenced on an Illumina NextSeq 550 following the manufacturer's instructions using a NextSeq 500/550 Mid or High Output kit (Illumina, 20024904 or 20024907). Reads were allocated as follows: I1, 8; I2, 8; R1, 150; and R2, 0.

Cloning. The AAV-BI30 rep-cap plasmid was generated by assembling an oligonucleotide (IDT) containing the AAV-BI30 DNA sequence (5′-AACAACTCAACCCGCGGCGGC-3′) into a synthesized kanamycin resistant rep-tTA-Cap helper (kiCAP-AAV-BI30; GenScript) containing a K449R point mutation in AAV9. The AAV-BR1 cap gene was synthesized and cloned into the same kiCAP-AAV backbone. To generate pAAV–CAG–NLS–GFP–miR122–WPRE gene fragments were synthesized (GenScript) and cloned into pAAV–CAG–mTurquoise2, a gift from Viviana Gradinaru (Addgene, 99122). pAAV–CAG–Cre–miR122–WPRE was cloned by amplifying Cre from pAAV–EF1a–Cre (Addgene, 55636), a gift from Karl Deisseroth, with (5′-GAATTGCGGCCCAACGGTACCATGCCCAAGAAGA AGAGGAAGGT-3′) and (5′-TGACAATGGTGTTTGACCGGTGAATTCTCAGTC ACCATCTTCGAGCAGTC-3′) and then cloned into the pAAV–CAG–NLS–GFP–miR122–WPRE backbone using the KpnI and EcoRI restriction sites.

Immunohistochemistry. Mice were deeply anesthetized with an intraperitoneal injection of a ketamine/xylazine solution and transcardially perfused with ~15 ml of room-temperature PBS followed by ~20 ml of ice-cold 4% PFA using a peristaltic pump set to a flow rate of ~9 ml min−1. Tissues were subsequently collected and processed as follows.

Pia vasculature whole mounts. Brain was dissected out of the skull and partially immersed in PBS in a glass dish. A razor blade was used to make a cut along the sagittal midline followed by a cut along the horizontal axis to separate each hemisphere into dorsal and ventral pieces. Dorsal-facing brain samples were then transferred into a 48-well plate and post-fixed in 4% PFA on ice for 30 min. All subsequent wash steps were carried out in the plate and care was taken to ensure the ventral surface of the brain sample always remained in contact with the bottom of the dish. Samples were washed 3× with PBS, blocked with a 10% donkey serum/0.5% PBST (Triton X-100) solution for 2 h at room temperature and then incubated with primary antibodies made up in blocking solution for 48 h at 4 °C with agitation. Next, samples were washed 3× with 0.5% PBST and 1× with PBS. To capture images, brain sample was placed dorsal side down in a two-well glass-bottom slide (Ibidi 80287) partially filled with PBS such that the pia vasculature faced the objective on an inverted microscope.

Aorta whole mounts. Thoracic aorta was grossly dissected and immersed in PBS. Fat, connective tissue and arterial branches were subsequently removed via fine dissection. A post-fixation step was omitted. Aortas were washed 3× with PBS, blocked with a 10% donkey serum 0.5% PBST solution for 1 h at room temperature and then incubated with primary antibodies made up in blocking solution overnight at 4 °C with agitation. Next, aortas were washed 3× with 0.5% PBST and immersed in PBS. A single cut was made lengthwise along the vessels to expose the lumen and the aortas were flat-mounted en face on glass coverslips.

Tissue sections. Organs were post-fixed in 4% PFA at 4 °C overnight. Alternatively, brain was post-fixed 4 h in 4% PFA on ice for caveolin-1 immunostaining due to fixation sensitivity of the antibody. Samples were then washed 3× with PBS to remove residual PFA. For cryosections, samples were cryopreserved in a 30% sucrose solution at 4 °C overnight and then frozen in NEG-50 (Richard-Allan Scientific 6502). The 18-µm (Figs. 1f, 3d and 4d and Extended Data Figs. 5 and 9) or 30-µm (Fig. 1c,e (BALB/cJ); Fig. 4b,c,e and Extended Data Figs. 2, 3, 4 (BALB/cJ), 6 and 8) sections were cut using a cryostat. For vibratome sections, 60-µm (Fig. 1b,e (rat), Extended Data Fig. 4 (rat) and Supplementary Fig. 3) or 100-µm (Fig. 1d and 4a and Supplementary Fig. 5) sections were cut using a LeicaVT1200S vibratome. Sections were washed 3× in PBS, permeabilized in 0.5% PBST for 10 min and then blocked with a 5% donkey serum/0.1% PBST solution for 1 h at room temperature. Sections were subsequently incubated with primary antibodies made up in blocking solution overnight at 4 °C, washed 3× with 0.1% PBST and incubated with secondary antibodies and DAPI made up in blocking solution for 1 h at room temperature. Finally, sections were washed 3× with 0.1% PBST, 1× with PBS and coverslipped for imaging.

Retina whole mounts. Eyes were removed from the eye sockets and briefly post-fixed in room-temperature 4% PFA for 5 min. Next, retinas were isolated via fine dissection in PBS and further post-fixed in room-temperature 4% PFA for 30 min. Retinas were washed 3× with PBS, blocked with a 10% donkey serum/0.5% PBST solution for 1 h at room temperature and then incubated with primary antibodies made up in blocking solution overnight at 4 °C with agitation. Next, retinas were washed 3× with 0.5% PBST, 1× with PBS and flat-mounted on glass coverslips.

The following primary antibodies were used at the indicated concentrations: rabbit anti-ERG, Alexa Fluor 647 (1:100 dilution; Abcam ab196149), rabbit anti-GFP, Alexa Fluor 488 (1:200 dilution; Thermo Fisher Scientific A-21311), mouse anti-α-SMA, FITC (1:500 dilution; Sigma-Aldrich F3777), mouse anti-α-SMA, Cy3 (1:500 dilution; Sigma-Aldrich C6198), mouse anti-α-SMA, Alexa Fluor 647 (1:100 dilution; Santa Cruz Biotechnology sc-32251), goat anti-CD31 (1:100 dilution; R&D Systems AF3628), rat anti-ICAM2 (1:100 dilution; BD Biosciences 553326), rabbit anti-caveolin-1 (1:200 dilution; Cell Signaling Technology 3267), mouse anti-RECA-1 (1:200 dilution; Abcam ab9774) and chicken anti-GFP (1:1,000 dilution; Aves Labs GFP-1020). In addition, isolectin GS-IB_4 and Alexa Fluor 568 (1:100 dilution; Invitrogen I21412) was used to stain vasculature in retina whole mounts. Specificity of the monoclonal anti-Cav1 antibody used in this study has been previously demonstrated by our group in caveolin-1 knockout mice[13].

Donkey anti-goat IgG, AF488 (1:250 dilution; Jackson ImmunoResearch 705-545-003), donkey anti-goat IgG, Cy3 (1:250 dilution; Jackson ImmunoResearch 705-165-147), donkey anti-rat IgG, AF488 pre-adsorbed against mouse IgG (1:250 dilution; Jackson ImmunoResearch 712-546-153), donkey anti-rat IgG, Cy3 pre-adsorbed against mouse IgG (1:250 dilution; Jackson ImmunoResearch 712-165-153), donkey anti-rabbit IgG, AF647 (1:250 dilution; Jackson ImmunoResearch 711-605-152), donkey anti-mouse IgG, AF546 highly cross-adsorbed (1:1,000 dilution; Invitrogen A10036) and goat anti-chicken, AF488 (1:1,000 dilution Invitrogen, A-11039) were used in conjunction with unconjugated primary antibodies.

Representative images were acquired with a Leica TCS SP8 confocal microscope, a Keyence BZ-X810 or a Nikon Ti-E inverted microscope/Andor CSU-X1 spinning disc confocal with an Andor DU-888 EMCCD camera.

Quantification of viral transduction efficiency. *NLS–GFP overexpression.* CellProfiler[65] was used to construct unbiased, semi-automated or fully automated analysis pipelines for all tissues examined. Viral transduction was assessed using a binary metric: GFP^+ERG^+ cells taken as a fraction of total ERG^+ cells. Staining and imaging of AAV-BI30 and AAV-BR1 samples was performed on the same day to ensure identical imaging conditions. All quantification was performed in C57BL/6NCrl mice. Retina, spinal cord and brain data were collected from the same set of animals. Tissue-specific workflow was as follows. Brain microvasculature. A single sagittal brain section was acquired from each animal and imaged in its entirety using an Olympus VS120 whole-slide-scanning microscope with a UPLSAPO ×20/0.75 objective lens. An average of 15,310 ± 3,929 (mean ± s.d.) endothelial cells were identified by the analysis pipeline in each replicate. Pia vasculature. Three ~1,164 µm × 1,164 µm fields of view (FOVs) of the pia vasculature were acquired for each animal using a Leica TCS SP8 confocal microscope with a HC PL APO ×10/0.40 objective lens. Relatively flat regions of the brain surface were sampled with shallow z-stacks to clearly separate pia vasculature from the underlying capillary plexus. Arteries and veins were manually identified using (1) the presence of α-SMA (high in arteries, low to absent in veins) and (2) the nuclear morphology of endothelial cells (ellipsoidal in arteries and circular in veins). Artery–vein overlap regions were omitted from analysis. Average endothelial cell counts identified by analysis pipeline per animal were as follows: 1,197 ± 182 (arterial endothelial cells), 1,908 ± 197 (venous endothelial cells). Retina vasculature. Organization of the retinal vasculature is highly stereotyped (vessels form three distinct vascular plexuses). Blood enters via the retinal artery, which emerges alongside the optic nerve, branching into spoke-like radial arteries that spread across the superficial plexus. These arteries elaborate to form a dense capillary network that constitute the majority of the intermediate and deep plexuses. Capillaries in the deep plexus finally merge into draining venules that ascend to the superficial plexus and form veins interleaved among the retina's arteries. To quantify viral transduction efficiency across the entirety of the retinal arterio–venous axis, four subregions of each retina whole-mount were sampled: radial arteries in the superficial plexus, capillaries in the intermediate plexus, capillaries in the deep plexus and radial veins in the superficial plexus. Three ~290 µm × 290 µm FOVs of each of these vascular subregions were acquired for each animal using a Leica TCS SP8 confocal microscope with an HC PL APO CS2 ×20/0.75 objective lens. Special care was taken when setting the *z* axis bounds on each image to isolate signal from a single vascular plexus. Superficial plexus arteries and veins within a given FOV were manually identified using SMA expression and nuclear morphology as described for pia vasculature. All ERG^+ nuclei within intermediate and deep plexus FOVs were counted; the vast majority of these endothelial cells belong to capillary microvessels. Average endothelial cell counts identified by analysis pipeline per animal were as follows: 155 ± 12 (superficial plexus arterial endothelial cells), 157 ± 13 (intermediate plexus endothelial cells), 229 ± 19 (deep plexus endothelial cells), 102 ± 11 (superficial plexus venous endothelial cells). Spinal cord microvasculature. Imaging was performed using a whole-slide-scanning microscope as described for the brain microvasculature. Images of two transverse sections were acquired for each animal and used to identify an average of 1,061 ± 200 endothelial cells in each replicate.

Non-endothelial transduction. (Fiji is Just) ImageJ's Cell Counter plugin was used to manually quantify non-endothelial transduction in cortex. These counts were collected from the aforementioned sagittal sections of brain used to quantify endothelial transduction efficiency in brain microvasculature (18-µm thick, imaged with an Olympus VS120 whole-slide-scanning microscope). $DAPI^+GFP^+ERG^-$ nuclei were identified as instances of non-endothelial transduction.

Ai9 recombination efficiency. Three ~582 µm × 582 µm FOVs of the cortical microvasculature per replicate were acquired from 30-µm sagittal sections using a Leica TCS SP8 confocal microscope with a HC PL APO CS2 ×20/0.75 objective lens. A modified Cell Profiler pipeline similar to those used to quantify AAV-mediated NLS–GFP overexpression was employed to count tdT^+ERG^+ cells taken as a fraction of total ERG^+ cells. An average of 481 ± 73 endothelial cells were identified by the analysis pipeline per replicate.

Cranial window implantation and two-photon imaging. The cranial window implantation workflow was based on the protocol described by Goldey et al.[66]. The craniotomy was centered over somatosensory cortex at approximately 2 mm posterior and 2.5 mm lateral to bregma. The perimeter of the craniotomy was traced using a 4-mm circular biopsy punch (VWR 21909-140) marked with a surgical marker (Aspen Surgical 1000-00-PDG). A custom titanium headplate was then centered on this trace and bonded to the skull with dental cement (C&B Metabond; Parkell S396, S398 and S371). Next, a micro-motor drill (Foredom, MH-170) outfitted with a 0.2-mm miniature carbide burr bit (Stoelting, 51451) was used to carefully remove the bone along the circumference of the craniotomy trace. The resulting circular bone flap was subsequently removed with fine forceps while continuously irrigating with saline to avoid damage to the pia vasculature. A cranial window composed of a 4-mm round cover glass (Warner Instruments CS-4, 64-0724) glued to a 5-mm round cover glass (Warner Instruments CS-5R, 64-0700) with a UV-curable adhesive (Norland Products NOA68) was carefully lowered onto the exposed brain and bonded to surrounding regions of the skull with dental cement. Finally, a well composed of O-Rings (USA Sealing, ZUSAH1X10 and ZUSAH1X10.5) adhered to one another with cyanoacrylate (3M Vetbond) was constructed around the window to facilitate use of a water-immersion objective. Immediately before imaging, 1 mg of 70 kDa Dextran and Texas Red (Thermo Fisher D1830) was dissolved in 75 µl sterile saline and injected intravenously via the tail vein to visualize the vasculature. In vivo imaging was performed with a previously described custom-built two-photon microscope[13] using a Mai Tai Ti:Sapphire (Spectra-Physics) laser tuned to 900 nm and ScanImage 5.1 (Vidrio Technologies).

Image processing and data analysis. (Fiji is Just) ImageJ 2.0.0-rc-69 and Adobe Illustrator 24.2 were used to process images displayed in figures throughout the manuscript. In cases where AAVs were directly compared, matched images were treated identically. GraphPad Prism v.9.1.1 was used for statistical analysis and graph generation.

Statistics and reproducibility. No statistical method was used to predetermine sample size. Sample size was instead designed to approximately match similar studies characterizing engineered AAVs[1,4,6]. All attempts at replication were successful and no data were excluded from the analyses. All replicates were assigned to treatment groups at random. Investigators were not blinded to allocation during experiments and outcome assessment.

Reporting Summary. Further information on research design is available in the Nature Research Reporting Summary linked to this article.

Data availability

Statistical data used to generate the graphs presented throughout the manuscript are provided in the form of source data and supplementary statistical data files. The kiCAP-AAV-BI30, NLS-GFP-miR122-WPRE-pA and pAAV-CAG-Cre-miR122-WPRE-pA plasmids generated in this study have been deposited in the Addgene repository under identification numbers 183749, 183775 and 183776, respectively.

Received: 4 August 2021; Accepted: 8 March 2022;
Published online: 13 April 2022

References

1. Deverman, B. E. et al. Cre-dependent selection yields AAV variants for widespread gene transfer to the adult brain. *Nat. Biotechnol.* **34**, 204–209 (2016).
2. Körbelin, J. et al. A brain microvasculature endothelial cell-specific viral vector with the potential to treat neurovascular and neurological diseases. *EMBO Mol. Med.* **8**, 609–625 (2016).

3. Tervo, D. G. R. et al. A designer AAV variant permits efficient retrograde access to projection neurons. *Neuron* **92**, 372–382 (2016).
4. Chan, K. Y. et al. Engineered AAVs for efficient noninvasive gene delivery to the central and peripheral nervous systems. *Nat. Neurosci.* **20**, 1172–1179 (2017).
5. Hanlon, K. S. et al. Selection of an efficient AAV vector for robust CNS transgene expression. *Mol. Ther. Methods Clin. Dev.* **15**, 320–332 (2019).
6. Kumar, S. R. et al. Multiplexed Cre-dependent selection yields systemic AAVs for Targeting distinct brain cell types. *Nat. Methods* **17**, 541–550 (2020).
7. Nonnenmacher, M. et al. Rapid evolution of blood–brain-barrier-penetrating AAV capsids by RNA-driven biopanning. *Mol. Ther. Methods Clin. Dev.* **20**, 366–378 (2020).
8. Sweeney, M. D., Kisler, K., Montagne, A., Toga, A. W. & Zlokovic, B. V. The role of brain vasculature in neurodegenerative disorders. *Nat. Neurosci.* **21**, 1318–1331 (2018).
9. Mastorakos, P. & McGavern, D. The anatomy and immunology of vasculature in the central nervous system. *Sci. Immunol.* **4**, eaav0492 (2019).
10. Vanlandewijck, M. et al. A molecular atlas of cell types and zonation in the brain vasculature. *Nature* **554**, 475–480 (2018).
11. Chen, B. R., Kozberg, M. G., Bouchard, M. B., Shaik, M. A. & Hillman, E. M. A critical role for the vascular endothelium in functional neurovascular coupling in the brain. *J. Am. Heart Assoc.* **3**, e000787 (2014).
12. Longden, T. A. et al. Capillary K^+-sensing initiates retrograde hyperpolarization to increase local cerebral blood flow. *Nat. Neurosci.* **20**, 717–726 (2017).
13. Chow, B. W. et al. Caveolae in CNS Arterioles mediate neurovascular coupling. *Nature* **579**, 106–110 (2020).
14. Ben-Zvi, A. et al. Mfsd2a is critical for the formation and function of the blood–brain barrier. *Nature* **509**, 507–511 (2014).
15. Andreone, B. J. et al. Blood–brain barrier permeability is regulated by lipid transport-dependent suppression of caveolae-mediated transcytosis. *Neuron* **94**, 581–594 (2017).
16. Chow, B. W. & Gu, C. Gradual suppression of transcytosis governs functional blood–retinal barrier formation. *Neuron* **93**, 1325–1333 (2017).
17. Kerfoot, S. M. & Kubes, P. Overlapping roles of P-selectin and α4 integrin to recruit leukocytes to the central nervous system in experimental autoimmune encephalomyelitis. *J. Immunol.* **169**, 1000–1006 (2002).
18. Piccio, L. et al. Molecular mechanisms involved in lymphocyte recruitment in inflamed brain microvessels: critical roles for P-selectin glycoprotein ligand-1 and heterotrimeric G(i)-linked receptors. *J. Immunol.* **168**, 1940–1949 (2002).
19. Tan, C. et al. Endothelium-derived semaphorin 3g regulates hippocampal synaptic structure and plasticity via neuropilin-2/plexinA4. *Neuron* **101**, 920–937 (2019).
20. Santisteban, M. M. et al. Endothelium-macrophage crosstalk mediates blood–brain barrier dysfunction in hypertension. *Hypertension* **76**, 795–807 (2020).
21. Liu, X. X. et al. Endothelial Cdk5 deficit leads to the development of spontaneous epilepsy through CXCL1/CXCR2-mediated reactive astrogliosis. *J. Exp. Med.* https://doi.org/10.1084/jem.20180992 (2020).
22. Dogbevia, G., Grasshoff, H., Othman, A., Penno, A. & Schwaninger, M. Brain endothelial-specific gene therapy improves experimental Sandhoff disease. *J. Cereb. Blood Flow Metab.* **40**, 1338–1350 (2020).
23. Chen, D. Y. et al. Endothelium-derived semaphorin 3G attenuates ischemic retinopathy by coordinating β-catenin-dependent vascular remodeling. *J. Clin. Invest.* **131**, e135296 (2021).
24. Nikolakopoulou, A. M. et al. Endothelial LRP1 protects against neurodegeneration by blocking cyclophilin A. *J. Exp. Med.* **218**, e20202207 (2021).
25. Cui, Y. et al. Brain endothelial PTEN/AKT/NEDD4-2/MFSD2A axis regulates blood–brain barrier permeability. *Cell Rep.* **36**, 109327 (2021).
26. Song, X. et al. Genome editing with AAV-BR1-CRISPR in postnatal mouse brain endothelial cells. *Int. J. Biol. Sci.* **18**, 652–660 (2022).
27. Tabebordbar, M. et al. Directed evolution of a family of AAV capsid variants enabling potent muscle-directed gene delivery across species. *Cell* **184**, 4919–4938 (2021).
28. Huang, Q. et al. Delivering genes across the blood–brain barrier: LY6A, a novel cellular receptor for AAV-PHP.B capsids. *PLoS ONE* **14**, e0225206 (2019).
29. Hordeaux, J. et al. The GPI-linked protein LY6A drives AAV-PHP.B transport across the blood–brain barrier. *Mol. Ther.* **27**, 912–921 (2019).
30. Lagos-Quintana, M. et al. Identification of tissue-specific microRNAs from mouse. *Curr. Biol.* **12**, 735–739 (2002).
31. Suzuki, T. et al. miR-122a-regulated expression of a suicide gene prevents hepatotoxicity without altering antitumor effects in suicide gene therapy. *Mol. Ther.* **16**, 1719–1726 (2008).
32. Xie, J. et al. MicroRNA-regulated, systemically delivered rAAV9: a step closer to CNS-restricted transgene expression. *Mol. Ther.* **19**, 526–535 (2011).
33. Geisler, A. et al. microRNA122-regulated transgene expression increases specificity of cardiac gene transfer upon intravenous delivery of AAV9 vectors. *Gene Ther.* **18**, 199–209 (2011).
34. Hordeaux, J. et al. The neurotropic properties of AAV-PHP.B are limited to C57BL/6J mice. *Mol. Ther.* **26**, 664–668 (2018).
35. Matsuzaki, Y. et al. Intravenous administration of the adeno-associated virus-PHP.B capsid fails to upregulate transduction efficiency in the marmoset brain. *Neurosci. Lett.* **665**, 182–188 (2018).
36. dela Paz, N. G. & D'Amore, P. A. Arterial versus venous endothelial cells. *Cell Tissue Res.* **335**, 5–16 (2008).
37. Shah, A. V., Birdsey, G. M. & Randi, A. M. Regulation of endothelial homeostasis, vascular development and angiogenesis by the transcription factor ERG. *Vasc. Pharmacol.* **86**, 3–13 (2016).
38. Graßhoff, H. et al. Short regulatory DNA sequences to target brain endothelial cells for gene therapy. *J. Cereb. Blood Flow Metab.* https://doi.org/10.1177/0271678X211039617 (2021).
39. Hill, R. A. et al. Regional blood flow in the normal and ischemic brain is controlled by arteriolar smooth muscle cell contractility and not by capillary pericytes. *Neuron* **87**, 95–110 (2015).
40. Bartanusz, V., Jezova, D., Alajajian, B. & Digicaylioglu, M. The blood–spinal cord barrier: morphology and clinical implications. *Ann. Neurol.* **70**, 194–206 (2011).
41. Stahl, A. et al. The mouse retina as an angiogenesis model. *Invest. Ophthalmol. Vis. Sci.* **51**, 2813–2826 (2010).
42. Newman, E. A. Functional hyperemia and mechanisms of neurovascular coupling in the retinal vasculature. *J. Cereb. Blood Flow Metab.* **33**, 1685–1695 (2013).
43. Hobson, B. & Denekamp, J. Endothelial proliferation in tumours and normal tissues: continuous labelling studies. *Br. J. Cancer* **49**, 405–413 (1984).
44. Madisen, L. et al. A robust and high-throughput Cre reporting and characterization system for the whole mouse brain. *Nat. Neurosci.* **13**, 133–140 (2010).
45. Razani, B. et al. Caveolin-1 null mice are viable but show evidence of hyperproliferative and vascular abnormalities. *J. Biol. Chem.* **276**, 38121–38138 (2001).
46. Asterholm, I. W., Mundy, D. I., Weng, J., Anderson, R. G. W. & Scherer, P. E. Altered mitochondrial function and metabolic inflexibility associated with loss of caveolin-1. *Cell Metab.* **15**, 171–185 (2012).
47. Nitta, T. et al. Size-selective loosening of the blood-brain barrier in claudin-5-deficient mice. *J. Cell Biol.* **161**, 653–660 (2003).
48. Stenman, J. M. et al. Canonical Wnt signaling regulates organ-specific assembly and dizfferentiation of CNS vasculature. *Science* **322**, 1247–1250 (2008).
49. Liebner, S. et al. Wnt/β-catenin signaling controls development of the blood–brain barrier. *J. Cell Biol.* **183**, 409–417 (2008).
50. Daneman, R. et al. Wnt/β-catenin signaling is required for CNS, but not non-CNS, angiogenesis. *Proc. Natl Acad. Sci. USA* **106**, 641–646 (2009).
51. Tran, K. A. et al. Endothelial β-catenin signaling is required for maintaining adult blood–brain barrier integrity and central nervous system homeostasis. *Circulation* **133**, 177–186 (2016).
52. Kalucka, J. et al. Single-cell transcriptome atlas of murine endothelial cells. *Cell* **180**, 764–779 (2020).
53. Wang, Y. et al. Ephrin-B2 controls VEGF-induced angiogenesis and lymphangiogenesis. *Nature* **465**, 483–486 (2010).
54. Kisanuki, Y. Y. et al. Tie2-Cre transgenic mice: a new model for endothelial cell-lineage analysis in vivo. *Dev. Biol.* **230**, 230–242 (2001).
55. Pu, W. et al. Mfsd2a$^+$ hepatocytes repopulate the liver during injury and regeneration. *Nat. Commun.* **7**, 13369 (2016).
56. Ridder, D. A. et al. TAK1 in brain endothelial cells mediates fever and lethargy. *J. Exp. Med.* **208**, 2615–2623 (2011).
57. Sawada, Y. et al. High transgene expression by lentiviral vectors causes maldevelopment of Purkinje cells in vivo. *Cerebellum* **9**, 291–302 (2010).
58. Khabou, H., Cordeau, C., Pacot, L., Fisson, S. & Dalkara, D. Dosage thresholds and influence of transgene cassette in adeno-associated virus-related toxicity. *Hum. Gene Ther.* **29**, 1235–1241 (2018).
59. Goertsen, D. et al. AAV capsid variants with brain-wide transgene expression and decreased liver targeting after intravenous delivery in mouse and marmoset. *Nat. Neurosci.* https://doi.org/10.1038/s41593-021-00969-4 (2021).
60. Ehling, M., Adams, S., Benedito, R. & Adams, R. H. Notch controls retinal blood vessel maturation and quiescence. *Development* **140**, 3051–3061 (2013).
61. Batista, A. R. et al. Ly6a differential expression in blood–brain barrier is responsible for strain specific central nervous system transduction profile of AAV-PHP.B. *Hum. Gene Ther.* **31**, 90–102 (2020).
62. Tabebordbar, M. et al. In vivo gene editing in dystrophic mouse muscle and muscle stem cells. *Science* **351**, 407–411 (2016).
63. Levy, J. M. et al. Cytosine and adenine base editing of the brain, liver, retina, heart and skeletal muscle of mice via adeno-associated viruses. *Nat. Biomed. Eng.* **4**, 97–110 (2020).
64. Challis, R. C. et al. Systemic AAV vectors for widespread and targeted gene delivery in rodents. *Nat. Protoc.* **14**, 379–414 (2019).
65. McQuin, C. et al. CellProfiler 3.0: next-generation image processing for biology. *PLoS Biol.* **16**, e2005970 (2018).

66. Goldey, G. J. et al. Removable cranial windows for long-term imaging in awake mice. *Nat. Protoc.* **9**, 2515–2538 (2014).
67. DiMattia, M. A. et al. Structural insight into the unique properties of adeno-associated virus serotype 9. *J. Virol.* **86**, 6947–6958 (2012).

Acknowledgements

We thank members of the Gu and Deverman laboratories for their insightful feedback throughout the study and their comments on the manuscript during drafting. This research was supported by a National Science Foundation Graduate Research Fellowship (grant no. DGE1745303) (T.K.), an HMS Mahoney Postdoctoral Fellowship (L.K.), an award from the National Institutes of Health (NIH) Common Fund and the National Institute of Neurological Disorders and Stroke through the Somatic Cell Genome Engineering Consortium (UG3NS111689) (B.D.), a Brain Initiative award funded through the National Institute of Mental Health (UG3MH120096) (B.D.), the Stanley Center for Psychiatric Research (B.D.), a Fidelity Biosciences Research Initiative (C.G.), an Allen Distinguished Investigator Award (C.G.), an AHA-Allen Initiative in Brain Health and Cognitive Impairment Award (C.G.), NIH R35NS116820 (C.G), NIH RF1DA048786 (C.G.) and NIH R01 HL153261 (C.G.). The research of C.G. was supported in part by a Faculty Scholar grant from the Howard Hughes Medical Institute. C.G. is an investigator of the Howard Hughes Medical Institute. Imaging was in part performed in the Neurobiology Imaging Facility at Harvard Medical School. This facility is supported in part by the HMS/BCH Center for Neuroscience Research as part of an NINDS P30 Core Center grant (NS072030).

Author contributions

T.K., K.C., C.G. and B.D. conceived the study and interpreted the results. T.K., K.C., L.K., Q.H., J.W., Q.Z., T.B., I.T., S.P., Y.C. and D.R. performed experiments. V.K. and A.C. assisted with data processing. T.K., K.C., L.K., J.W., Y.C. and B.D. prepared the figures. T.K. wrote the manuscript with input from K.C., B.D. and C.G. and editing from L.K. and Y.C. C.G. and B.D. supervised the project. All authors discussed the experiments and read and approved the manuscript.

Competing interests

K.C., Q.H. and B.D. are inventors on a provisional patent application filed by the Broad Institute (applicant). The specific aspects of the manuscript covered include modified AAV vectors and methods of making and using the same. B.D. is a scientific founder and scientific advisor of Apertura Gene Therapy. B.D. receives research funding from Apertura Gene Therapy, which was used to generate some of the data in this manuscript. B.D. is on the scientific advisory board of Tevard Biosciences. The remaining authors declare no competing interests.

Additional information

Extended data is available for this paper at https://doi.org/10.1038/s44161-022-00046-4.

Supplementary information The online version contains supplementary material available at https://doi.org/10.1038/s44161-022-00046-4.

Correspondence and requests for materials should be addressed to Chenghua Gu or Benjamin E. Deverman.

Peer review information *Nature Cardiovascular Research* thanks the anonymous reviewers for their contribution to the peer review of this work.

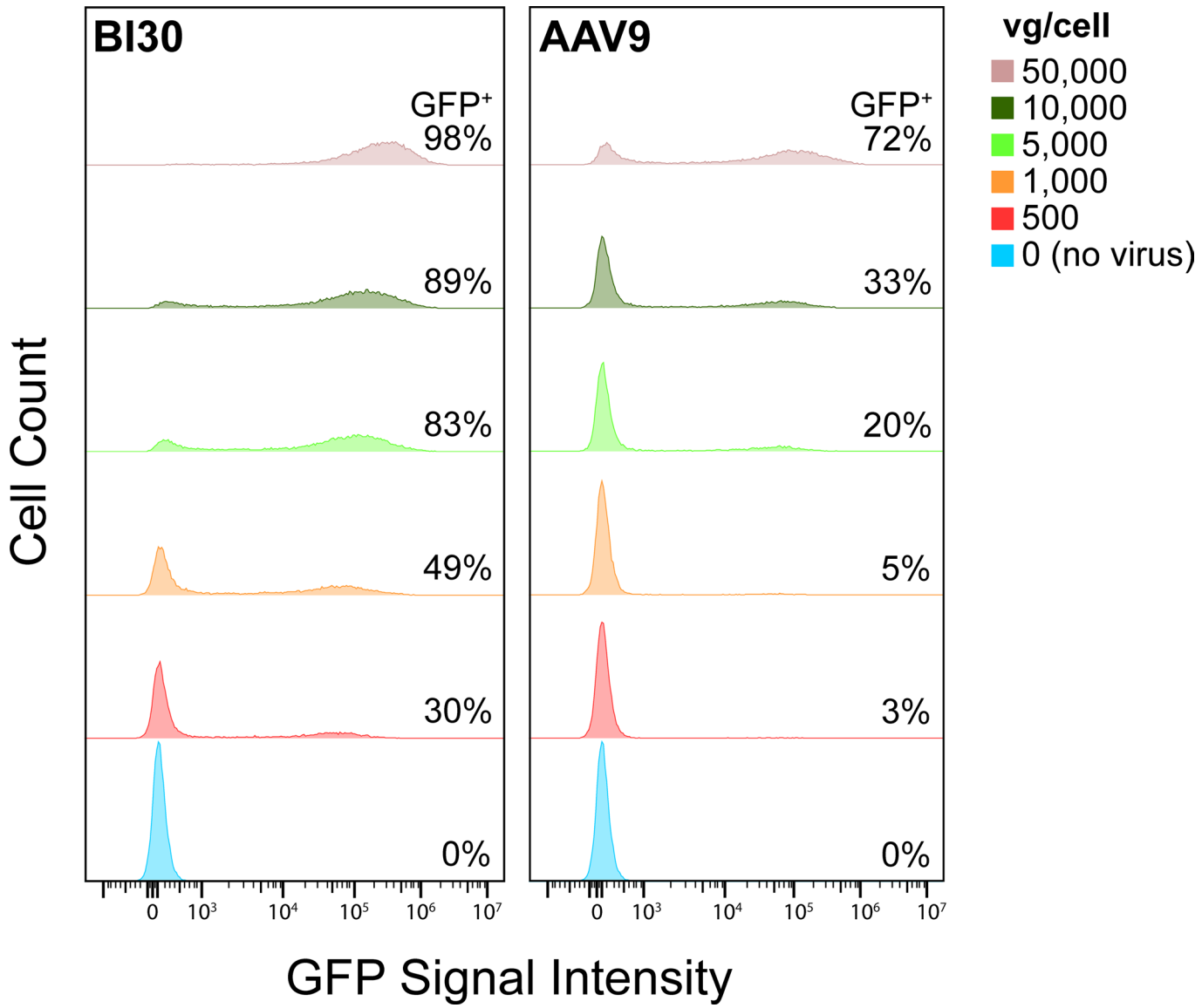

Extended Data Fig. 1 | AAV-BI30 is more efficient at transducing hCMEC/D3 cells than AAV9 across a wide range of doses. hCMEC/D3 cells were grown to confluence in a 24-well plate format. AAV9 or AAV-BI30 carrying a CAG-NLS-GFP-miR122-WPRE genome was applied to cells at 0, 500, 1,000, 5,000, 10,000, or 50,000 vg/cell. 4 days post-treatment the cells were analyzed for GFP expression via flow cytometry. The profiles show data from a single sample from each condition but are representative of $n = 2$ replicates.

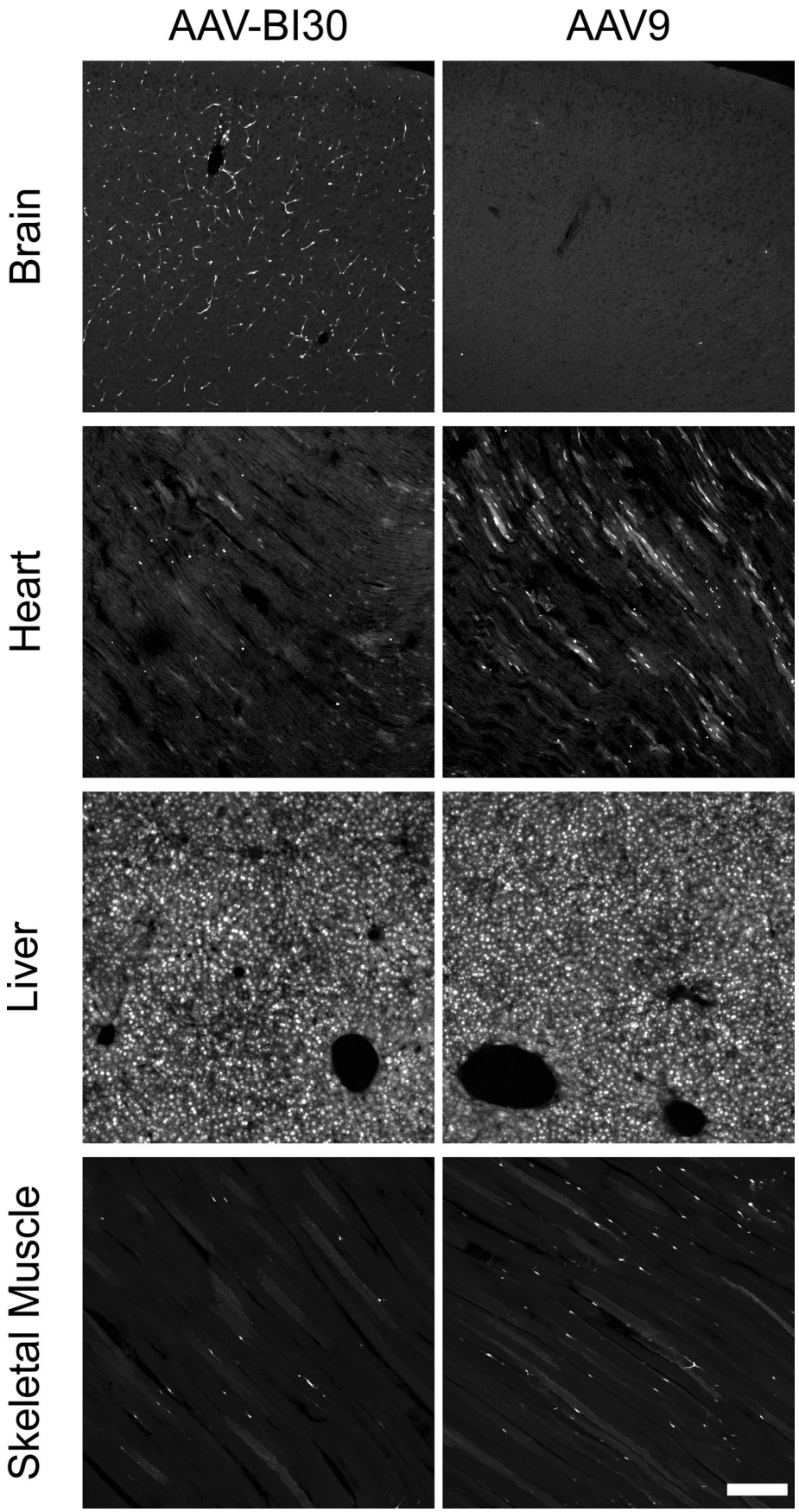

Extended Data Fig. 2 | See next page for caption.

Extended Data Fig. 2 | Comparison of the tropism of AAV-BI30 and AAV9. AAV-BI30 or AAV9 vectors carrying a CAG-NLS-GFP-WPRE genome were intravenously administered to adult C57BL/6 mice at 1×10^{11} vg/animal and transduction was assessed after 7 days. Panels show endogenous NLS-GFP transgene expression in organs throughout the body. Scale bar shown is 200 μm. Images are representative of $n=3$ animals per group.

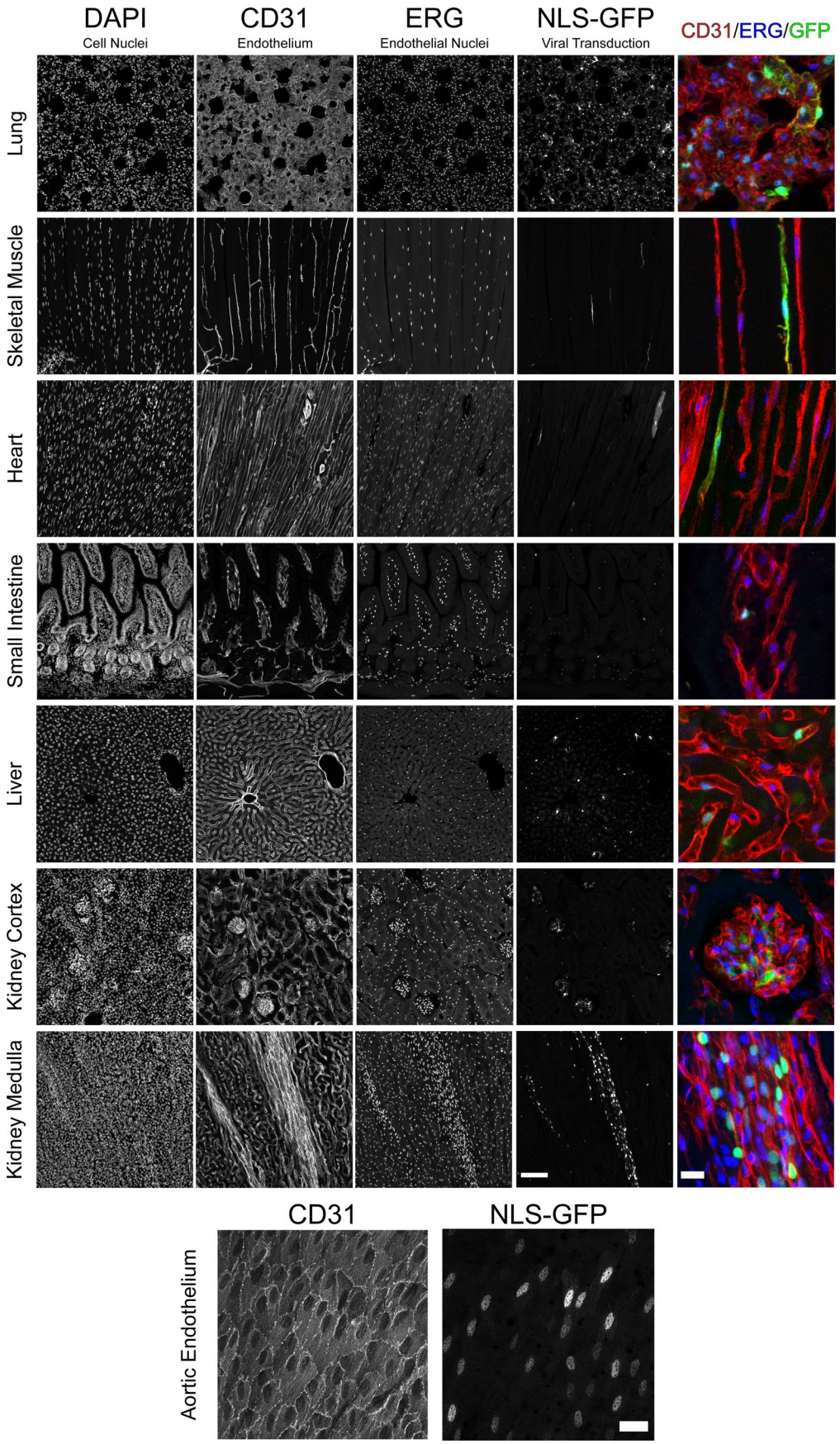

Extended Data Fig. 3 | See next page for caption.

Extended Data Fig. 3 | Characterization of the peripheral tropism of AAV-BI30. AAV-BI30:CAG-NLS-GFP-miR122-WPRE was intravenously administered to adult C57BL/6 mice at 1×10^{11} vg/animal and transduction was assessed after three weeks. Representative images of AAV-BI30 transduction throughout the periphery; high-zoom colocalization of GFP with endothelial markers is shown in the rightmost column. With the notable exception of lung, AAV-BI30 rarely transduced endothelial cells in the microvasculature of peripheral organs – a striking contrast to efficient transduction seen throughout the CNS vasculature. Note residual NLS-GFP expression in hepatocytes of the liver persisting in the presence of miR122 repeats in the viral genome, illustrating AAV-BI30's potent transduction of this cell type. Transduction observed in kidney glomeruli was non-endothelial; GFP^+ cells are most likely mesangial cells. Relatively strong endothelial transduction in the interlobular vessels of the renal medulla and the aorta suggest that AAV-BI30 may achieve transduction of large-diameter arteries and veins throughout the systemic circulation. Scale bars are as follows: 100 μm in fourth column from left, 15 μm in rightmost column, and 25 μm in aorta panel. Images are representative of $n=3$ animals.

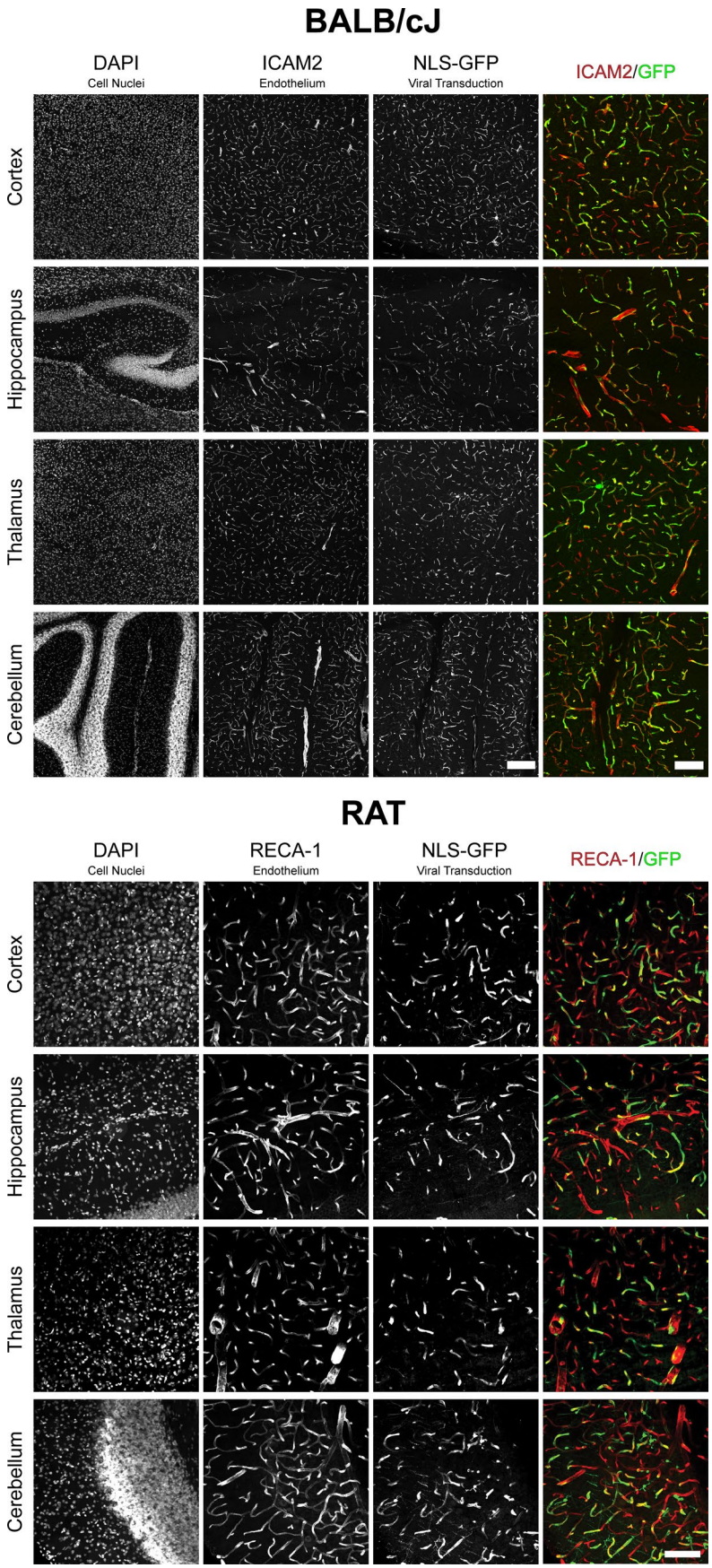

Extended Data Fig. 4 | See next page for caption.

Extended Data Fig. 4 | AAV-BI30 transduces endothelial cells throughout the BALB/cJ and rat brain. AAV-BI30:CAG-NLS-GFP-miR122-WPRE was intravenously administered at 1×10^{11} vg/animal (BALB/cJ; top) or 1.42×10^{13} vg/kg (rat; bottom). Transduction was assessed after three (BALB/cJ) or four (rat) weeks. Images demonstrate endothelial expression of NLS-GFP transgene throughout brains of each species. Scale bars shown are 200 µm (BALB/cJ third row from left) or 100 µm (BALB/cJ rightmost row & rat). Images are representative of $n=3$ BALB/cJ mice, $n=1$ rat.

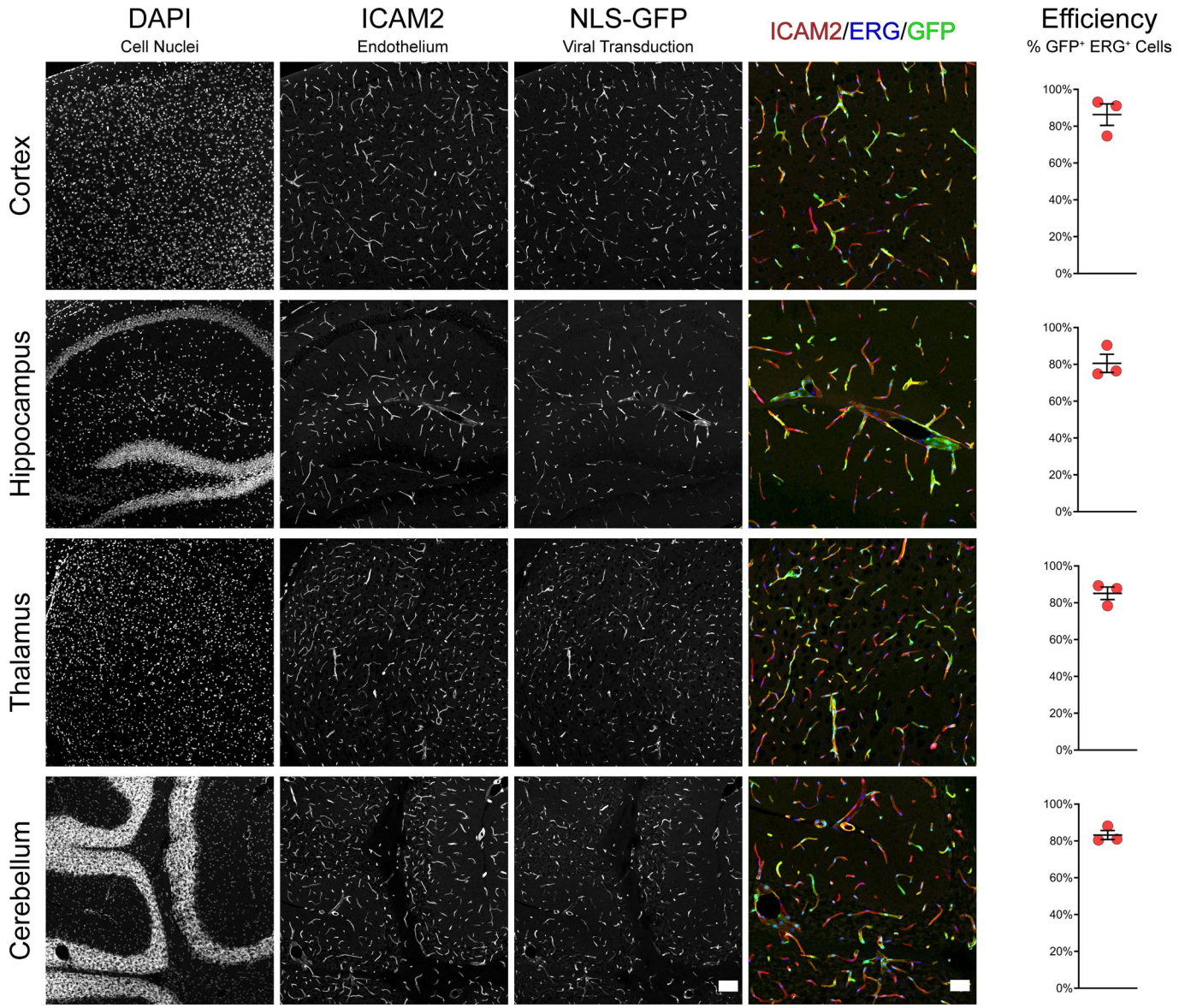

Extended Data Fig. 5 | Endothelial transduction by AAV-BI30 is consistent across brain regions. AAV-BI30:CAG-NLS-GFP-miR122-WPRE was intravenously administered to adult C57BL/6 mice at 1×10^{11} vg/animal and transduction was assessed after three weeks. Images demonstrate high endothelial expression of NLS-GFP transgene throughout the brain. Region-specific endothelial transduction efficiency was as follows: $86\pm6\%$ in cortex, $81\pm5\%$ in hippocampus, $85\pm3\%$ in thalamus, $83\pm2\%$ in cerebellum (mean $\pm$ s.e.m.; $n=3$ animals). Compare to $84\pm4\%$ efficiency measured across entire brain. Scale bars are as follows: third row from left 100 μm; rightmost row 50 μm.

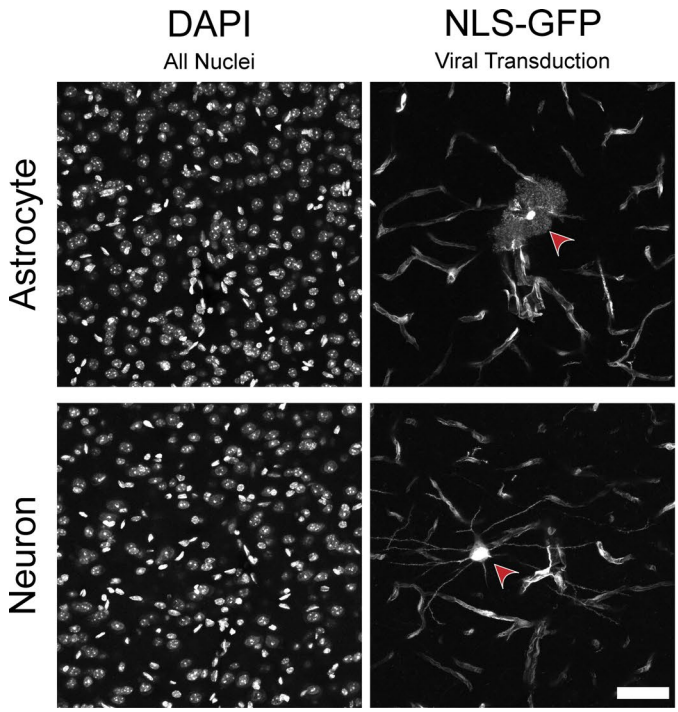

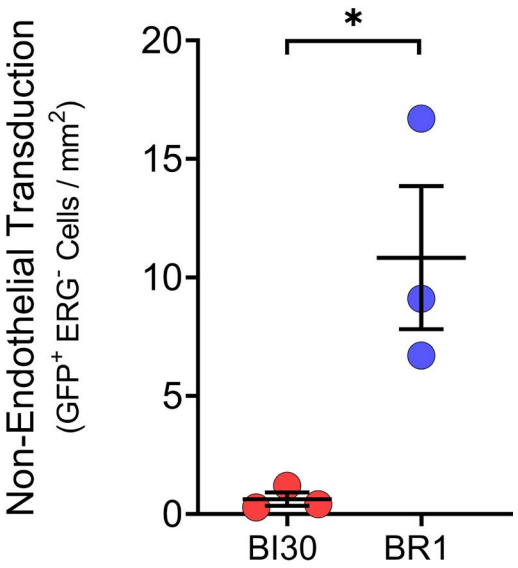

Extended Data Fig. 6 | The transduction profile of AAV-BI30 within the brain is highly endothelial-specific. AAV-BI30 or AAV-BR1 vectors carrying a CAG-NLS-GFP-miR122-WPRE genome were intravenously administered to adult C57BL/6 mice at 1×10^{11} vg/animal and transduction was assessed after three weeks. Left: Representative images of rare instances of neuronal and astrocytic transduction observed following AAV-BI30 administration at the 1×10^{11} vg/animal dose; cell types of interest are demarcated with red arrowheads. Scale bar shown is 50 μm. Right: Quantification of AAV transduction in non-endothelial (GFP^+ ERG^-) cells per mm^2 of cortex using 18 μm sagittal sections of brain. An average of 0.6 ± 0.3 and 10.8 ± 3.0 cells / mm^2 (mean ± s.e.m.; $n=3$ animals per group) were identified in AAV-BI30 and AAV-BR1 administered cohorts, respectively. Consistent with previous reports, neurons constituted the majority of non-endothelial cells transduced by AAV-BR1. The data presented were compared using an unpaired, two-tailed *t*-test ($t_4=3.37$; $P=0.0281$).

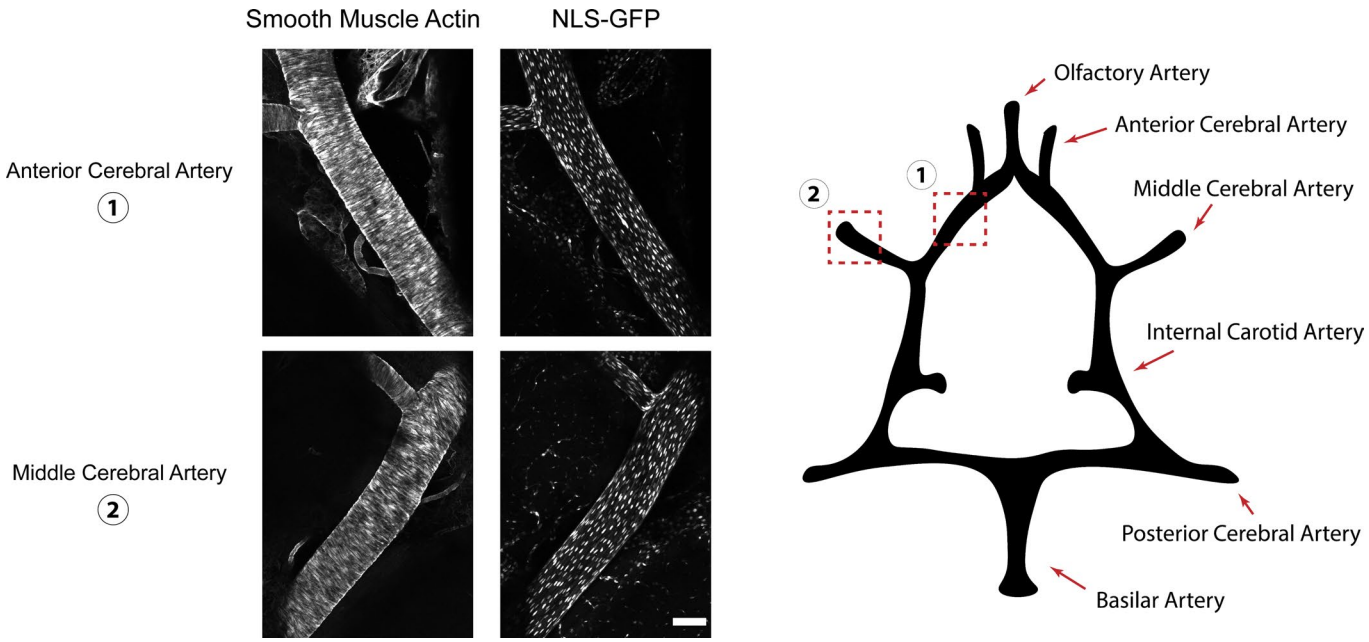

Extended Data Fig. 7 | AAV-BI30 efficiently transduces the brain's largest arteries. AAV-BI30:CAG-NLS-GFP-miR122-WPRE was intravenously administered to an adult C57BL/6 mouse at 5×10^{11} vg/animal and transduction was assessed after 3 weeks. Robust, endothelial-specific transduction was observed throughout the cerebral arteries, Circle of Willis, and the head of the basilar artery. Scale bar shown is 100 μm. Images are representative of $n=1$ mouse.

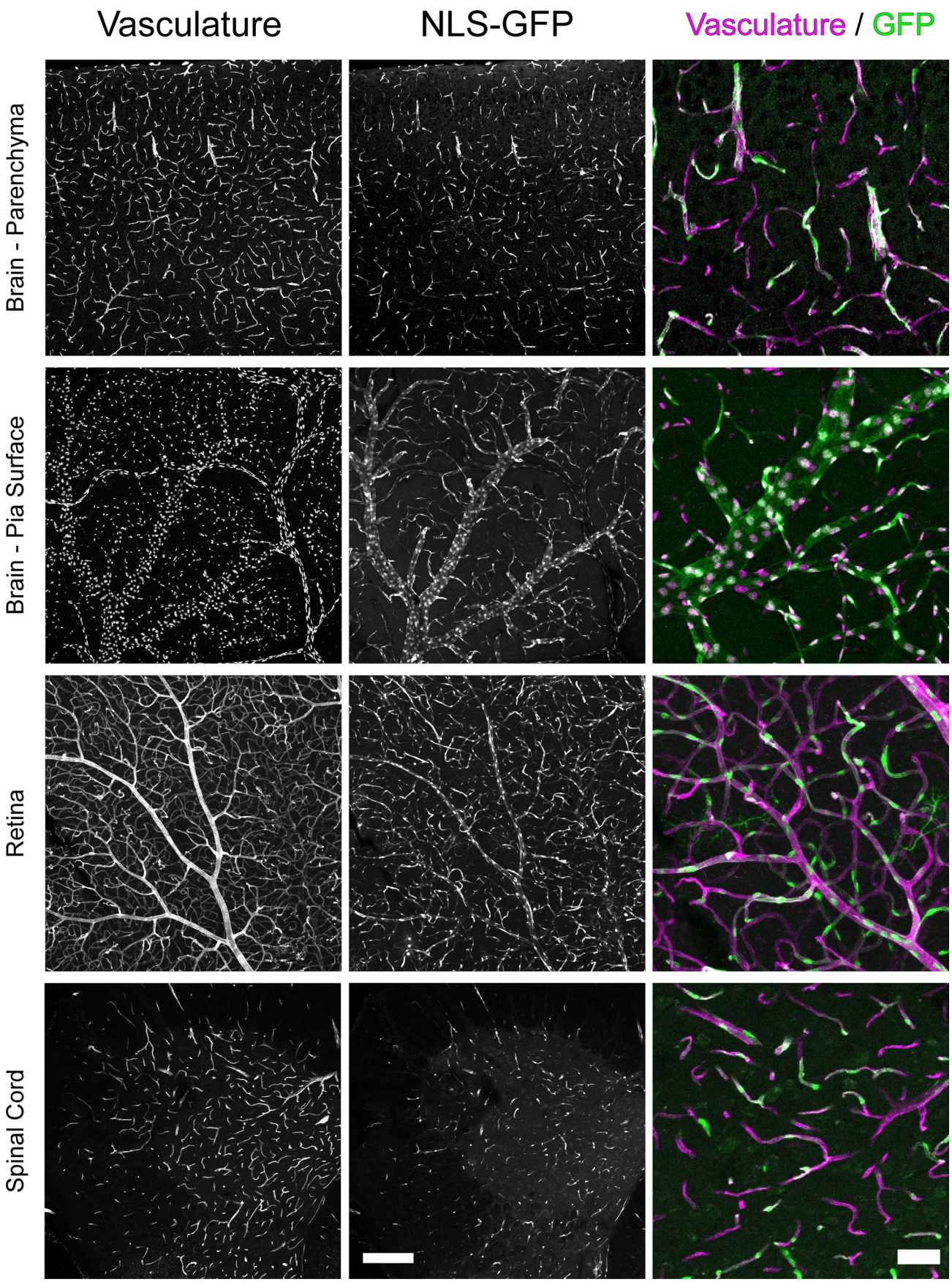

Extended Data Fig. 8 | See next page for caption.

Extended Data Fig. 8 | AAV-BI30-mediated gene transfer enables long-term transgene expression in CNS endothelial cells. AAV-BI30:CAG-NLS-GFP-miR122-WPRE was intravenously administered to adult C57BL/6 mice at 1×10^{11} vg/animal and transduction was assessed after approximately 5 months (152 days). Vascular counterstains displayed are as follows: ICAM2 in brain parenchyma and spinal cord; isolectin in retina; and ERG in pia vasculature. High-zoom colocalization with GFP shown in rightmost column. Scale bars are as follows: middle row 200 μm; rightmost row 50 μm. Images are representative of $n=3$ mice.

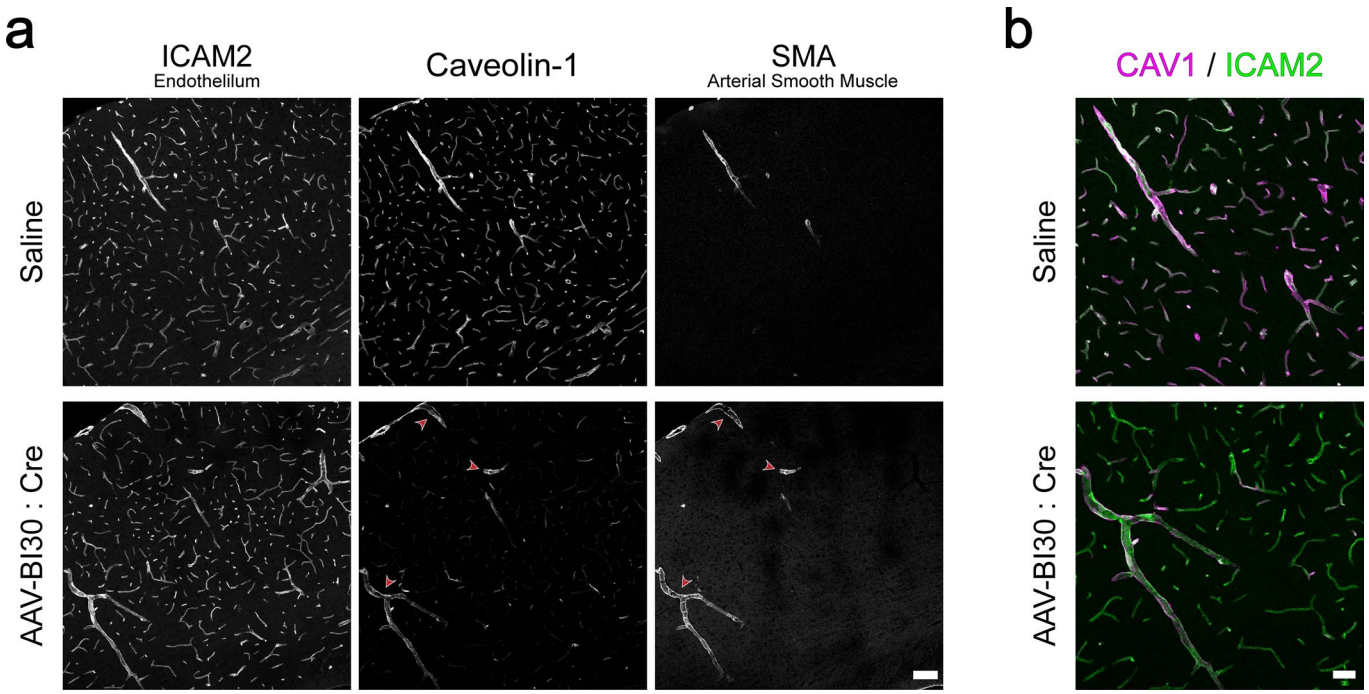

Extended Data Fig. 9 | AAV-BI30-mediated Cre delivery achieves efficient endothelial-specific gene deletion. A 1×10^{11} vg/animal dose of AAV-BI30:CAG-Cre-miR122-WPRE or saline was intravenously administered to adult $Cav1^{fl/fl}$ mice, and Caveolin-1 protein levels were assessed after four weeks. Representative images of the brain microvasculature show strongly reduced endothelial Caveolin-1 protein levels in AAV-BI30 injected animals. Note lack of Caveolin-1 loss in the smooth muscle cell layer of arterioles, demarcated with red arrowheads. High-zoom colocalization of Caveolin-1 and ICAM2 shown in rightmost column. Scale bars are as follows: second column from right 100 μm; rightmost column 50 μm. Images are representative of $n=3$ mice per group.

Capsid	Parental Vector	Peptide Insertion	Dominant CNS Tropism	Enhanced Transduction in BALBc/J Strain?	Enhanced Transduction in Human Endothelial Cell Lines?	References
BI30	AAV9	NNSTRGG	Endothelial Cells	Yes	Yes - (hBMVECs & hCMEC/D3)	
PHP.V1	AAV9	TALKPFL	Endothelial Cells, Astrocytes	No	Yes - (HBMEC)	[1]
PHP.V2	AAV9	TTLKPFL	Endothelial Cells, Astrocytes	Unknown	Unknown	[1]
PHP.eB	AAV-PHP.B	[DG]TLAVPFK	Neurons, Astrocytes, Oligodendrocytes, Endothelial Cells	No	No - (hBMVECs & hCMEC/D3)	[2], Fig 1A
PHP.B	AAV9	TLAVPFK	Neurons, Astrocytes, Oligodendrocytes, Endothelial Cells	No	Unknown	[3]
BR1	AAV2	NRGTEWD	Endothelial Cells	Unknown	No - (hCMEC/D3)	[4]
PPS	AAV2	DSPAHPS	Endothelial Cells	Unknown	No - (hCMEC/D3)	[5], [4]

References

[1] S. R. Kumar *et al.*, "Multiplexed Cre-Dependent Selection Yields Systemic AAVs for Targeting Distinct Brain Cell Types," *Nat Methods*, vol. 17, no. 5, pp. 541–550, 2020.
[2] K. Y. Chan *et al.*, "Engineered AAVs for Efficient Noninvasive Gene Delivery to the Central and Peripheral Nervous Systems," *Nat Neurosci*, vol. 20, no. 8, pp. 1172–1179, 2017.
[3] B. E. Deverman *et al.*, "Cre-Dependent Selection Yields AAV Variants for Widespread Gene Transfer to the Adult Brain," *Nat Biotechnol*, vol. 34, no. 2, pp. 204–209, 2016.
[4] J. Körbelin *et al.*, "A Brain Microvasculature Endothelial Cell-Specific Viral Vector With the Potential to Treat Neurovascular and Neurological Diseases," *EMBO Mol Med*, vol. 8, no. 6, pp. 609–25, 2016.
[5] Y. H. Chen, M. Chang, and B. L. Davidson, "Molecular Signatures of Disease Brain Endothelia Provide New Sites for CNS-Directed Enzyme Therapy," *Nat Med*, vol. 15, no. 10, pp. 1215–1219, 2009.

Extended Data Fig. 10 | Comparison of engineered AAV capsids with enhanced CNS endothelial cell transduction. The heptameric peptides used to generate the listed capsids were uniformly inserted within the surface exposed hypervariable region VIII of the AAV sequence[67]. Specifically, heptamers are inserted between amino acids 587 & 588 in AAV-PPS and 588 & 589 in AAVs BI30, BR1, PHP.B, PHP.V1, and PHP.V2. AAV-PHP.eB shares AAV-PHP.B's TLAVPFK insert and additionally contains an AQ to DG mutation at amino acids 587-588 (bracketed sequence).

nature portfolio

Corresponding author(s): Chenghua Gu and Benjamin E Deverman

Last updated by author(s): Apr 5, 2022

Reporting Summary

Nature Portfolio wishes to improve the reproducibility of the work that we publish. This form provides structure for consistency and transparency in reporting. For further information on Nature Portfolio policies, see our Editorial Policies and the Editorial Policy Checklist.

Statistics

For all statistical analyses, confirm that the following items are present in the figure legend, table legend, main text, or Methods section.

n/a	Confirmed
☐	☒ The exact sample size (*n*) for each experimental group/condition, given as a discrete number and unit of measurement
☐	☒ A statement on whether measurements were taken from distinct samples or whether the same sample was measured repeatedly
☐	☒ The statistical test(s) used AND whether they are one- or two-sided *Only common tests should be described solely by name; describe more complex techniques in the Methods section.*
☒	☐ A description of all covariates tested
☒	☐ A description of any assumptions or corrections, such as tests of normality and adjustment for multiple comparisons
☐	☒ A full description of the statistical parameters including central tendency (e.g. means) or other basic estimates (e.g. regression coefficient) AND variation (e.g. standard deviation) or associated estimates of uncertainty (e.g. confidence intervals)
☐	☒ For null hypothesis testing, the test statistic (e.g. *F*, *t*, *r*) with confidence intervals, effect sizes, degrees of freedom and *P* value noted *Give P values as exact values whenever suitable.*
☒	☐ For Bayesian analysis, information on the choice of priors and Markov chain Monte Carlo settings
☒	☐ For hierarchical and complex designs, identification of the appropriate level for tests and full reporting of outcomes
☒	☐ Estimates of effect sizes (e.g. Cohen's *d*, Pearson's *r*), indicating how they were calculated

Our web collection on statistics for biologists contains articles on many of the points above.

Software and code

Policy information about availability of computer code

Data collection	ScanImage 5.1 was used for two-photon imaging (Vidrio Technologies). FlowJo 10.8.1 (BD Biosciences) was used for flow cytometry.
Data analysis	Cell Profiler (an open-source image analysis software) was used to quantify viral transduction as described in the Methods. Additional details concerning the software are described in McQuin, C. et al. CellProfiler 3.0: Next-Generation Image Processing for Biology. PLoS Biol 16, e2005970 (2018). Cell Profiler documentation, support, and download are available at https://cellprofiler.org/. (Fiji is Just) ImageJ 2.0.0-rc-69 and Adobe Illustrator 24.2 were used to process images and assemble figures. GraphPad Prism 9.1.1 was used to perform statistical tests and generate graphs.

For manuscripts utilizing custom algorithms or software that are central to the research but not yet described in published literature, software must be made available to editors and reviewers. We strongly encourage code deposition in a community repository (e.g. GitHub). See the Nature Portfolio guidelines for submitting code & software for further information.

Data

Policy information about availability of data

All manuscripts must include a data availability statement. This statement should provide the following information, where applicable:

- Accession codes, unique identifiers, or web links for publicly available datasets
- A description of any restrictions on data availability
- For clinical datasets or third party data, please ensure that the statement adheres to our policy

Statistical data used to generate the graphs presented throughout the manuscript is provided in the form of Source Data and Supplementary Statistical Data files. The kiCAP-AAV-BI30, NLS-GFP-miR122-WPRE-pA, and pAAV-CAG-Cre-miR122-WPRE-pA plasmids generated in this study have been deposited in the Addgene repository under identification numbers 183749, 183775, and 183776 respectively.

Field-specific reporting

Please select the one below that is the best fit for your research. If you are not sure, read the appropriate sections before making your selection.

☒ Life sciences ☐ Behavioural & social sciences ☐ Ecological, evolutionary & environmental sciences

For a reference copy of the document with all sections, see nature.com/documents/nr-reporting-summary-flat.pdf

Life sciences study design

All studies must disclose on these points even when the disclosure is negative.

Sample size	Sample size was designed to approximately match recently published studies characterizing novel engineered AAVs. For example, see: Deverman, B. E. et al. Cre-Dependent Selection Yields AAV Variants for Widespread Gene Transfer to the Adult Brain. Nat Biotechnol 34, 204–209 (2016); Chan, K. Y. et al. Engineered AAVs for Efficient Noninvasive Gene Delivery to the Central and Peripheral Nervous Systems. Nat Neurosci 20, 1172–1179 (2017); Kumar, S. R. et al. Multiplexed Cre-Dependent Selection Yields Systemic AAVs for Targeting Distinct Brain Cell Types. Nat Methods 17, 541–550 (2020).
Data exclusions	No data was excluded from the analyses.
Replication	All attempts at replication were successful.
Randomization	All replicates were assigned to treatment groups at random.
Blinding	Blinding was not performed. In the instances where treatment groups were compared (BI30 vs. BR1) the effect size - and hence sample identity - was immediately discernible by eye. However, to eliminate potential bias during quantitative measurement of AAV transduction, images were processed using an identical semi-autonomous pipeline described in the Methods.

Reporting for specific materials, systems and methods

We require information from authors about some types of materials, experimental systems and methods used in many studies. Here, indicate whether each material, system or method listed is relevant to your study. If you are not sure if a list item applies to your research, read the appropriate section before selecting a response.

Materials & experimental systems

n/a	Involved in the study
☐	☒ Antibodies
☐	☒ Eukaryotic cell lines
☒	☐ Palaeontology and archaeology
☐	☒ Animals and other organisms
☒	☐ Human research participants
☒	☐ Clinical data
☒	☐ Dual use research of concern

Methods

n/a	Involved in the study
☒	☐ ChIP-seq
☐	☒ Flow cytometry
☒	☐ MRI-based neuroimaging

Antibodies

Antibodies used

All antibodies used in this study are commercially available:

Rabbit anti-ERG ◦ Alexa Fluor 647 (1:100; Abcam ab196149) - clone EPR3864
Rabbit anti-GFP ◦ Alexa Fluor 488 (1:200; Thermo Fisher Scientific A-21311) - lot #2207528
Mouse anti-α Smooth Muscle Actin ◦ Cy3 (1:500; Sigma-Aldrich C6198) - clone 1A4
Chicken anti-GFP (1:1000; Aves Labs GFP-1020) - lot #GFP879484
Mouse anti-α Smooth Muscle Actin ◦ Alexa Fluor 647 (1:100; Santa Cruz Biotechnology sc-32251) - clone 1A4
Goat anti-CD31 (1:100; R&D Systems AF3628) - several lots used simultaneously due to extremely high demand for this antibody
Rat anti-ICAM2 (1:100; BD Biosciences 553326) - clone 3C4(mIC2/4)
Mouse anti-RECA-1 (1:200; Abcam ab9774) - clone RECA-1
Rabbit anti-Caveolin-1 (1:200; Cell Signaling Technology 3267) - clone D46G3

Donkey anti-Goat IgG ◦ AF488 (1:250; Jackson ImmunoResearch 705-545-003)
Donkey anti-Goat IgG ◦ Cy3 (1:250; Jackson ImmunoResearch 705-165-147)
Donkey anti-Rat IgG ◦ AF488 pre-adsorbed against Mouse IgG (1:250; Jackson ImmunoResearch 712-546-153)
Donkey anti-Rat IgG ◦ Cy3 pre-adsorbed against Mouse IgG (1:250; Jackson ImmunoResearch 712-165-153)
Donkey anti-Rabbit IgG ◦ AF647 (1:250; Jackson ImmunoResearch 711-605-152)
Donkey anti-Mouse IgG ◦ AF546 highly cross-adsorbed (1:1000; Invitrogen A10036)
Goat anti-Chicken ◦ AF488 (1:1000 Invitrogen, A-11039)

Validation	Antibodies were exclusively used for immunohistochemistry. With the exception of anti-Caveolin-1, a knockout-validated antibody (see Chow, B. W. et al. Caveolae in CNS Arterioles Mediate Neurovascular Coupling. Nature 579, 106–110 (2020)), immunostaining was only used to identify endothelial cells and vessel segments of interest; no biological claims concerning the molecules targeted during immunization are made. As shown in representative images throughout our manuscript, the distribution and morphology of the cells detected via immunostaining confirms their suitability for this purpose. Furthermore, all reagents used have been extensively characterized in the vascular biology field (for example, see Vanlandewijck, M. et al. A Molecular Atlas of Cell Types and Zonation in the Brain Vasculature. Nature 554, 475–480 (2018)) Additional information on species cross-reactivity and specific references can be found on supplier websites.

Eukaryotic cell lines

Policy information about cell lines

Cell line source(s)	Human embryonic kidney 293 clone 17 [HEK 293T/17] from ATCC (CRL-11268) Human brain microvascular endothelial cells [hBMVEC] from CellBiologics (H-6023) Mouse brain microvascular endothelial cells [mBMVEC] from CellBiologics (C57-6023) Blood-brain barrier hCMEC/D3 cells from Millipore-Sigma (SCC066)
Authentication	None performed.
Mycoplasma contamination	Confirmed negative with Lonza Myco Alert Mycoplasma Detection Kit.
Commonly misidentified lines (See ICLAC register)	No commonly misidentified cell lines were used in this study.

Animals and other organisms

Policy information about studies involving animals; ARRIVE guidelines recommended for reporting animal research

Laboratory animals	The following commercially available mouse strains were used: C57BL/6NCrl (Charles River 027), C57BL/6J (Jackson Laboratory 000664), BALB/cJ (Jackson Laboratory 000651), and Ai9 (Jackson Laboratory 007909; originally generated by Madisen et al. 47). CD® (Sprague Dawley) IGS rat was obtained from Charles River (Strain Code 001). Cav1 flox mice were originally generated by Asterholm et al. and generously shared by Philipp Scherer. (see Asterholm, I. W., et al. Altered Mitochondrial Function and Metabolic Inflexibility Associated with Loss of Caveolin-1. Cell Metab 15, 171–185 (2012)) Recombinant AAV vectors were administered intravenously via the tail vein or retro-orbital sinus in young adult male or female animals (8 to 20 weeks old).
Wild animals	The study did not involve wild animals.
Field-collected samples	The study did not involve field-collected samples.
Ethics oversight	All procedures were approved by the Harvard University and Broad Institute of MIT and Harvard Institutional Animal Care and Use Committees (IACUC).

Note that full information on the approval of the study protocol must also be provided in the manuscript.

Flow Cytometry

Plots

Confirm that:

☒ The axis labels state the marker and fluorochrome used (e.g. CD4-FITC).

☒ The axis scales are clearly visible. Include numbers along axes only for bottom left plot of group (a 'group' is an analysis of identical markers).

☐ All plots are contour plots with outliers or pseudocolor plots.

☐ A numerical value for number of cells or percentage (with statistics) is provided.

Methodology

Sample preparation	A single flow cytometry experiment is described in this study (Extended Data Figure 1). Briefly, hCMEC/D3 cells were grown to confluence in a 24-well plate format. AAV9 or AAV-BI30 carrying a CAG-NLS-GFP-miR122-WPRE genome was applied to cells at 0, 500, 1,000, 5,000, 10,000, or 50,000 vg/cell. 4 days post-treatment the cells were analyzed for GFP expression.
Instrument	Beckman CytoFLEX S Flow Cytometer
Software	FlowJo 10.8.1
Cell population abundance	A pure hCMEC/D3 population was used as an input; 15,000 single cells were counted and analyzed per replicate. A numerical value for the percentage of GFP+ cells in each condition is provided in Extended Data Figure 1. However, statistics are not

provided because the experiment was only repeated for an n=2 with qualitatively similar results as specified in the figure legend.

Gating strategy

Gating was performed to select for cell viability (FSC/SSC) and singlets (FSC-A/FSC-H). The GFP positivity threshold was set at 10e3.

☒ Tick this box to confirm that a figure exemplifying the gating strategy is provided in the Supplementary Information.